Cross-checking SMBH mass estimates in NGC 6958-I. Stellar dynamics from adaptive optics-assisted MUSE observations

Monthly Notices of the ROYAL ASTRONOMICAL SOCIETY

MNRAS **509,** 5416–5436 (2022) https://doi.org/10.1093/mnras/stab3210
Advance Access publication 2021 November 10

Cross-checking SMBH mass estimates in NGC 6958 – I. Stellar dynamics from adaptive optics-assisted MUSE observations

Sabine Thater [1,2★] Davor Krajnović,[2] Peter M. Weilbacher,[2] Dieu D. Nguyen [3,4] Martin Bureau,[5,6] Michele Cappellari [5] Timothy A. Davis [7] Satoru Iguchi [8] Richard McDermid,[9,10] Kyoko Onishi,[11] Marc Sarzi[12] and Glenn van de Ven[1]

[1]*Department of Astrophysics, University of Vienna, Türkenschanzstraße 17, A-1180 Vienna, Austria*
[2]*Leibniz Institute for Astrophysics Potsdam (AIP), An der Sternwarte 16, D-14482 Potsdam, Germany*
[3]*Department of Physics, International University, Quarter 6, Linh Trung Ward, Thu Duc City, Ho Chi Minh City, Vietnam*
[4]*Vietnam National University, Ho Chi Minh City, Vietnam*
[5]*Sub-department of Astrophysics, Department of Physics, University of Oxford, Denys Wilkinson Building, Keble Road, Oxford OX13RH, UK*
[6]*Yonsei Frontier Lab and Department of Astronomy, Yonsei University, 50 Yonsei-ro, Seodaemun-gu, Seoul 03722, Republic of Korea*
[7]*School of Physics and Astronomy, Cardiff University, Queens Buildings, The Parade, Cardiff CF24 3AA, UK*
[8]*National Astronomical Observatory of Japan (NAOJ), National Institute of Natural Sciences (NINS), 2-21-1 Osawa, Mitaka, Tokyo 181-8588, Japan*
[9]*Department of Physics and Astronomy, Macquarie University, Macquarie Park, NSW 2109, Australia*
[10]*Astronomy, Astrophysics and Astrophotonics Research Centre, Macquarie University, Sydney, NSW 2109, Australia*
[11]*Department of Space, Earth and Environment, Chalmers University of Technology, Onsala Observatory, SE-439 92 Onsala, Sweden*
[12]*Armagh Observatory and Planetarium, College Hill, Armagh BT61 9DG, UK*

Accepted 2021 November 2. Received 2021 November 2; in original form 2021 May 13

ABSTRACT

Supermassive black hole masses ($M_{\rm BH}$) can dynamically be estimated with various methods and using different kinematic tracers. Different methods have only been cross-checked for a small number of galaxies and often show discrepancies. To understand these discrepancies, detailed cross-comparisons of additional galaxies are needed. We present the first part of our cross-comparison between stellar- and gas-based $M_{\rm BH}$ estimates in the nearby fast-rotating early-type galaxy NGC 6958. The measurements presented here are based on ground-layer adaptive optics-assisted Multi-Unit Spectroscopic Explorer (MUSE) science verification data at around 0.″6 spatial resolution. The spatial resolution is a key ingredient for the measurement and we provide a Gaussian parametrization of the adaptive optics-assisted point spread function for various wavelengths. From the MUSE data, we extracted the stellar kinematics and constructed dynamical models. Using an axisymmetric Schwarzschild technique, we measured an $M_{\rm BH}$ of $(3.6^{+2.7}_{-2.4}) \times 10^8\,{\rm M}_\odot$ at 3σ significance taking kinematical and dynamical systematics (e.g. radially varying mass-to-light ratio) into account. We also added a dark halo, but our data do not allow us to constrain the dark matter fraction. Adding dark matter with an abundance matching prior results in a 25 per cent more massive black hole. Jeans anisotropic models return $M_{\rm BH}$ of $(4.6^{+2.5}_{-2.7}) \times 10^8$ and $(8.6^{+0.8}_{-0.8}) \times 10^8\,{\rm M}_\odot$ at 3σ confidence for spherical and cylindrical alignments of the velocity ellipsoid, respectively. In a follow-up study, we will compare the stellar-based $M_{\rm BH}$ with those from cold and warm gas tracers, which will provide additional constraints for the $M_{\rm BH}$ for NGC 6958, and insights into assumptions that lead to potential systematic uncertainty.

Key words: galaxies: individual: NGC 6958 – galaxies: kinematics and dynamics – galaxies: nuclei.

1 INTRODUCTION

The developments in astronomical instrumentation over the last two decades have substantially improved the capability of astronomical observations: Remarkably, it is now possible to robustly measure the mass of supermassive black holes (SMBH) in nearby galaxies with a precision of less than a factor of 2 using a variety of different methods (e.g. review by Kormendy & Ho 2013). Determining robust black hole masses is a challenging task that requires the best possible spatial resolution for both photometric and spectroscopic observations and sophisticated modelling methods. As black holes are per se not visible, we need to trace the motion of the material that is sensitive to the gravitational potential of the SMBH. Popular tracers are individual stars (in the Milky Way; Ghez et al. 2008; Gillessen et al. 2009, 2017), masers (e.g. Miyoshi et al. 1995; Kuo et al. 2011; Greene et al. 2016; Gao & Ho 2017), ionized (e.g. Beifiori et al. 2012; Walsh et al. 2013), molecular (e.g. Davis et al. 2013, 2018, 2020; Onishi et al. 2015, 2017; Boizelle et al. 2019, 2021; Nguyen et al. 2020, 2021a), or atomic gas (Nguyen et al. 2021b), and unresolved stellar systems (e.g. Rusli et al. 2013; Saglia et al. 2016; Nguyen et al. 2017, 2018, 2019; Krajnović et al. 2018; Thater et al. 2019). While a variety of different tracers and methods are available, it is not possible to use a single modelling method to measure $M_{\rm BH}$ for all

★ E-mail: sabine.thater@univie.ac.at

different types of galaxies. Stellar-based methods can be best used for early-type galaxies that usually do not have strongly varying stellar populations nor subcomponents like bars or spiral arms. On the other hand, gas is typically found in late-type galaxies and can be used as a tracer if the gas follows circular orbits and is not strongly disturbed. Other methods require the presence of nuclear maser emission or an active galactic nucleus. Checks for inconsistencies between the different mass determination methods are important for identifying systematic uncertainties associated with the techniques and deriving robust massive black hole masses.

Hitherto, cross-checks between different dynamical modelling methods have only been performed for a handful of objects. While the checks give consistent results in a number of cases (Shapiro et al. 2006; Davies et al. 2007; Neumayer et al. 2007; Pastorini et al. 2007; Cappellari et al. 2009; van den Bosch & de Zeeuw 2010; Feldmeier et al. 2014; Feldmeier-Krause et al. 2017; Krajnović et al. 2018), many cross-checks reveal clear discrepancies (e.g. Ferrarese, Ford & Jaffe 1996; Verdoes Kleijn et al. 2002; de Francesco, Capetti & Marconi 2006; Gebhardt et al. 2011; Walsh et al. 2012, 2013; Onken et al. 2014; Barth et al. 2016; Boizelle et al. 2021). Fig. 2 in Thater et al. (2020) shows that $M_{\rm BH}$ determined from ionized and molecular gas-based measurements seem to be systematically lower than those derived from stellar dynamical models for $M_{\rm BH}$ greater than a few 10^8 $M_\odot$. The origin of these discrepancies cannot be pinned down easily, because different methods, assumptions, and wavelength ranges are used for different tracers, which probe the gravitational potential in different ways. The inhomogeneity of the mass measurements and the low-number statistics make it challenging to quantify the effect of the different methods on the scatter in $M_{\rm BH}$ scaling relations. Hence, providing a measure of the systematics from the different methods is mandatory for an in-depth understanding of the origin of the black hole relations and thus of the growth of SMBHs. Particularly, we need to answer the questions: How do systematics change the slope of the scaling relations? How much of the scatter in the black hole scaling relations can be attributed to inconsistencies between the various dynamical measurement methods?

As we slowly start to reach a statistically robust galaxy sample with measured $M_{\rm BH}$, now is the best time to revisit known black hole mass measurements with different methods for two reasons. First, the high spatial resolution of the *Hubble Space Telescope (HST)* allowed for a systematic determination of $M_{\rm BH}$ in a large sample of galaxies. Still, the usage of long-slit rather than modern integral-field spectroscopy limited the precision of early measurements. The spatial resolution achieved by adding adaptive optics (AO) to integral-field spectroscopy was another substantial step forward in measuring black hole masses (e.g. Krajnović et al. 2005). Secondly, even most recent dynamical mass measurements are affected by systematic biases associated with the modelling assumptions. Discussed are for example radially varying versus constant mass-to-light ratio (M/L; Thater et al. 2017, 2019), the inclusion of dark matter (Gebhardt & Thomas 2009; Rusli et al. 2013), radially varying versus constant anisotropy (Drehmer et al. 2015), and axisymmetric versus triaxial shapes of galaxies (van den Bosch & de Zeeuw 2010; Ahn et al. 2018). It is thus essential to understand and quantify the systematics as detailed as possible, to evaluate the robustness of the mass measurements and mitigate the associated systematic uncertainties. We decided to perform this test by comparing the $M_{\rm BH}$ derived with the widely applied techniques of using stars, ionized gas, and molecular gas as tracers of the gravitational potential.

Table 1. Basic properties of NGC 6958.

Property		Notes
Morphological type	S0	1
Distance (Mpc)	35 ± 8	2
Physical scale (pc arcsec^{-1})	170 ± 10	–
Inclination (°)	45 ± 4	3
Position angle (°)	109 ± 5	4
Sersic index	3.3	5
Effective radius (kpc)	2.59	5
$\sigma_{\rm e,star}$ (km s^{-1})	168 ± 5	6
$\sigma_{\rm 0,star}$ (km s^{-1})	220 ± 5	6
Bulge mass ($M_\odot$)	$(3.6 \pm 1.4) \times 10^{10}$	7

Notes. 1: The galaxy was misclassified in de Vaucouleurs et al. (1991) and we adopt the classification by Sandage & Bedke (1994) and Laurikainen et al. (2010). 2: Mean distance based on dynamical scaling relations from the NASA/IPAC Extragalactic Database (NED). 3: Inclination of the molecular gas disc of NGC 6958 derived in the follow-up publication. 4: Derived from the MUSE velocity field within an FoV of 5 arcsec. 5: Derived from the light model in Section 4.1. 6: Derived by co-adding the spectra of the MUSE data cube in elliptical apertures with an ellipticity of 0.15 and a semimajor axis of the effective radius $R_{\rm eff}$ (15.″3) and $R_{\rm eff}/8 = 1.''9$, respectively. 7: Using the total mass derived from the Jeans Anisotropic models (Section 4.3) of this work and the bulge-to-total ratio (=0.45) from Laurikainen et al. (2010).

We first needed to identify a galaxy that offers the possibility to apply the different modelling methods. Early-type galaxies with bright nuclear molecular gas discs are prime candidates. We found such an object in the mm-Wave Interferometric Survey of Dark Object Masses sample (e.g. Davis et al. 2017, 2018; Onishi et al. 2017) that provides high-resolution Atacama Large Millimeter/submillimeter Array observations for a large variety of galaxies. In this work, we targeted the massive fast-rotating early-type galaxy NGC 6958, which shows clear signs of a regularly rotating nuclear molecular gas disc (see Thater et al. 2020). The main properties of NGC 6958 are given in Table 1.

NGC 6958 is an isolated galaxy (Madore, Freedman & Bothun 2004). There is evidence of a recent minor merger (Malin & Carter 1983; Saraiva, Ferrari & Pastoriza 1999; Tal et al. 2009), but the merger does not affect our $M_{\rm BH}$ measurement as the central stellar kinematics show very regular features (see Section 3). NGC 6958 was also classified as a low-ionization nuclear emission-line region galaxy showing large equivalent width of Hα and [N II]λ6584 emission lines (Saraiva et al. 2001; Annibali et al. 2010), which we will use to estimate $M_{\rm BH}$ accounting for the non-circular motions of the ionized gas via asymmetric drift correction. Based on the galaxy's effective velocity dispersion of 168 km s^{-1}, the $M_{\rm BH}$–$\sigma_{\rm e,star}$ relation (Saglia et al. 2016) predicts an SMBH of mass $M_{\rm BH} = 1.1 \times 10^8$ $M_\odot$ that at a rather uncertain distance of 35 Mpc (see Table 1) is at the limit to be detectable ($R_{\rm SoI,1e8\,M_\odot} = 0.''1$)[1] with AO-assisted and interferometric facilities. As shown in Fig. 2 of Thater et al. (2020), this is the mass region where gas- and stellar-based $M_{\rm BH}$ seem to be discrepant.

This publication is the first part of our study of using independent kinematic tracers to derive the black hole mass in NGC 6958 and check whether the different methods give consistent results. This paper will focus on the use of stars as dynamical tracers, and is composed of five sections. We begin by presenting the AO-assisted MUSE integral-field spectroscopic and *HST* photometric observations in Section 2. We then explain the stellar and ionized

[1]The SoI is defined as $R_{\rm SoI} = GM_{\rm BH}/\sigma^2_{\rm e,star}$, where G is the gravitational constant. Within $R_{\rm SoI}$, the gravitational potential is dominated by the SMBH.

gas kinematics extraction in Section 3, where we also include a detailed evaluation of the MUSE + AO point spread function (PSF). In Section 4, we derive the galaxy's stellar mass distribution and perform dynamical Jeans Anisotropic and Schwarzschild modelling of the stellar kinematics to obtain the massive black hole mass. We conclude this paper by putting our results in context with the $M_{\rm BH}$ scaling relations and providing a short outlook to the second paper in this series (Thater et al., in preparation).

2 OBSERVATIONS

2.1 MUSE integral-field spectroscopic data

We obtained AO-assisted Multi-Unit Spectroscopic Explorer (MUSE; Bacon et al. 2010) wide-field mode science verification data under the science programme 60.A-9193(A) (PI: Krajnović) at the Very Large Telescope (VLT) in the night of 2017 September 18. The Ground Atmospheric Layer Adaptive Optics for Spectroscopic Imaging (GALACSI) AO system (Ströbele et al. 2012) was developed to optimize the performance of MUSE and consists of four sodium laser guide stars, a deformable secondary mirror on the VLT UT4, and an infrared low-order sensor to provide near-diffraction-limited observations at visible wavelength. In addition to the four laser guide stars, we used a slow-guiding star 39 arcsec and a tip-tilt star 65 arcsec from the nucleus. Due to bad weather conditions during the observations,[2] we could not make use of the full AO capabilities and achieved a spatial resolution of 0.6 arcsec (Section 3.1). Our MUSE observations have a total exposure time of 2040 s divided into four 510 s on-source integrations observed in the sequence O–S–O–O–S–O, where O are the observations of the target and S of the sky.

We performed the data reduction using the MUSE data reduction pipeline (Weilbacher et al. 2020) version 2.6. The pipeline includes bias and sky subtraction, flat-field correction, wavelength, and flux calibration and telluric correction of each on-source observation. Furthermore, new with version 2.6, wiggles that are visible in the spectral direction of high signal-to-noise (S/N) data in MUSE AO observations are appropriately corrected for. After the data reduction, we merged the individual exposures with the MUSE pipeline, taking the respective offsets into account. In the final data cube, each spaxel has a size of 0.2 arcsec × 0.2 arcsec and spectral sampling of 1.25 Å. The total wavelength range covered by our data goes from 4700 to 9300 Å. However, during the observation, the spectral region between 5800 and 5970 Å was blocked by a NaD notch filter to avoid light contamination by the sodium lasers of the AO system and we do not have any spectral data in this region. The spectral resolution of the MUSE data varies between 2.5 and 2.9 Å (Guérou et al. 2017).

We show the white-light image of the MUSE observation of NGC 6958 covering the full field of view (FoV) of 1 arcmin × 1 arcmin in Fig. 1. In the following analysis, we used the central 30 arcsec × 30 arcsec of the MUSE FoV as we noted a kinematic twist for radii larger than 15 arcsec (whereas the kinematics are very regular within this radius). The cut-out MUSE data cube was then Voronoi binned (Cappellari & Copin 2003) to a target S/N of 70 Å^{-1} for each bin, resulting in mostly unbinned spaxels in the galaxy centre and bin sizes of 1–2 arcsec at a distance more than 7 arcsec from the centre. Fig. 1 also shows a bright star at a projected distance of about 20 arcsec away from the galaxy centre. We used this bright star for our PSF estimations in Section 3.1.

[2]https://www.eso.org/sci/activities/vltsv/musesv.html

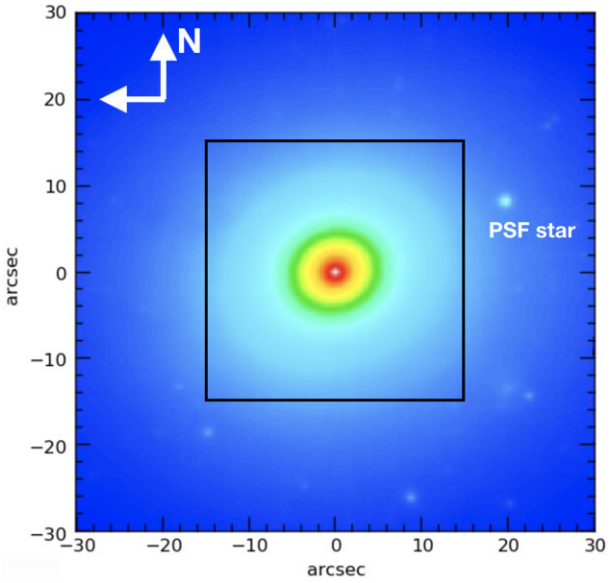

Figure 1. Full FoV white-light image of our MUSE observations covering 1 arcmin × 1 arcmin. The rectangle indicates the cut-out 30 arcsec × 30 arcsec FoV used in this study. The bright star in the north-west was used for the PSF estimations in Section 3.1. 10 arcsec corresponds to 1.7 kpc in physical scales.

2.2 Imaging data

NGC 6958 was observed with *HST* several times. In the archive, we found a 400 s exposure in the F814W band (PI: P. Goudfrooij, PID: 8686) obtained with the Wide Field Camera (WFC) of the Wide Field and Planetary Camera 2 (WFPC2; Holtzman et al. 1995) and a 1152 s exposure in the *H* band (F160W; PI: A. Capetti, PID: 11219) of the Near Infrared Camera and Multi-Object Spectrometer (NICMOS). NGC 6958 contains a nuclear dust disc, which is less impacted by dust attenuation when using a near-infrared image (F160W). In addition, the galaxy was only observed with one of the WFC chips of WFPC2, which has a lower sampling (0.″1 per pixel) than the NICMOS image (0.″076 per pixel).

The best possible spatial resolution and proper treatment of the nuclear dust are crucial for measuring the black hole mass in all applied dynamical methods discussed in this work. We therefore decided to use the F160W NICMOS imaging data for the main dynamical models and the image in the F814W band to test how alternative mass models affect our dynamical modelling results (see Section 4.4.3). Deeper large-scale images are additionally needed to trace the galactic gravitational potential up to large scales. This is important for the construction of the orbit library of the Schwarzschild models (Section 4.2). Here, we used an F160W Wide Field Camera 3 (WFC3) image of NGC 6958 (PI: B. Boizelle, PID: 15909) with a spatial sampling of (0.″13 per pixel), and an *i*-band image from the Carnegie Irvine Galaxy Survey (CGS) Project (Ho et al. 2011; Li et al. 2011; Huang et al. 2013).

3 STELLAR AND IONIZED GAS KINEMATICS

In this section, we will show the kinematic extraction of our ground-layer AO-assisted MUSE observations. So far, MUSE has only been used for two other black hole mass measurements (Mehrgan et al. 2019, den Brok et al. 2021) and this is the second paper to present a stellar-based massive black hole mass measurement using the AO mode of MUSE.

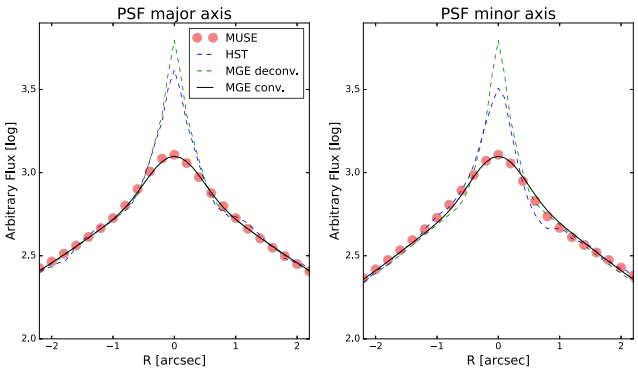

Figure 2. Spatial resolution of our MUSE observations derived by comparison of the MUSE white-light image with the *HST*/WFPC2/F814W image. We note that the dust contamination (well visible in the plot of the minor axis) can broaden the broad component of the Gaussian to unrealistic scales.

3.1 Spatial resolution in the GALACSI AO mode

The quality of the MUSE data can be assessed by estimating the spatial resolution, which is composed of the instrumental and atmospheric PSF. As the atmospheric PSF changes depending on the observational conditions, it needs to be carefully evaluated for each observation. This is a crucial step as the spatial resolution limits how far we can probe the dynamics in the centre of the galaxy. For determining the PSF, a typical method in dynamical $M_{\rm BH}$ estimation is to use a high-resolution image of the galaxy at similar wavelength and degrade it via PSF convolution until it matches the integrated light image of the integral-field unit (IFU) data (e.g. McDermid et al. 2006; Krajnović et al. 2009; Thater et al. 2017).

We first followed this approach by convolving the light model of the F814W WFPC2 image (derived in Appendix A) with a PSF parametrized as the sum of two concentric Gaussians (Fig. 2). We used the F814W image because it is closest to the wavelength of our MUSE observations. From the fit to the white-light image, we recovered a narrow component of the PSF of 0.″61. As the quality of the AO correction, and therefore the PSF, is wavelength dependent (Bacon et al. 2017), we derived the PSF for the different wavelength cuts that we used to extract the stellar kinematics (see Sections 3.2 and 4.4.1). The PSF fit is very sensitive to the dust content of the galaxy, and we noted large and unrealistic full width at half-maximum (FWHM) values (≈10 arcsec) for the broad Gaussian component in the optical and blue spectral region. We therefore carefully masked the dust-affected regions and chose (based on the results of the PSF star in the next subsection) an upper boundary of 1.″7 for the broad Gaussian. The PSF parametrizations of the different wavelength ranges used for the dynamical modelling are shown in Table 2.

An alternative approach is to fit the sum of two concentric Gaussians to one of the stars within the full FoV of our MUSE data cube. The brightest star in our FoV with a projected distance of 20 arcsec provides a good handle on the central PSF of our observations. We subtracted the galaxy light background and then fitted two concentric Gaussians to the PSF star profile along the x-axis and the y-axis. While the MUSE PSF is usually fitted with a MOFFAT profile (Moffat 1969), the two concentric Gaussians also well reproduce our PSF star profile. A few examples of the fit are shown in the appendix (Fig. B1) and the PSF parametrizations are also shown in Table 2. From the PSF star measurement in the white-light image, we derived a narrow Gaussian PSF of 0.″60 that is in agreement with the PSF that we measured using the nucleus of the galaxy.

Table 2. Gaussian parametrization of the MUSE PSF.

Method	Nucleus			Star		
Sp. range (Å)	$FWHM_1$ (arcsec)	$FWHM_2$ (arcsec)	*f1*	$FWHM_1$ (arcsec)	$FWHM_2$ (arcsec)	*f1*
(1)	(2)	(3)	(4)	(5)	(6)	(7)
4699–9298	0.61	1.69	0.48	0.60	1.32	0.64
4820–6820	0.99	0.99	0.93	0.69	1.41	0.62
4820–5750	0.64	1.69	0.29	0.72	1.43	0.57
8500–8800	0.57	1.41	0.49	0.56	1.30	0.72

Notes. Parametrization of the MUSE PSF as double Gaussian centred on the galaxy centre (columns 2–4) and double Gaussian centred on the PSF star (columns 5–7). In detail: Column 1: Spectral range collapsed for the integrated light image. The spectral regions are ordered as 'white-light', 'optical', 'blue', and calcium triplet (CaT) range. Columns 2, 3, 5, and 6: FWHM of the two Gaussians. Columns 4 and 7: Relative flux of the narrow Gaussian (G1).

Using the PSF star, we also measured the change of the PSF over the full wavelength range using 20 regularly and equally spaced wavelength channels (of 500 Å width). In Fig. 3, we show the average of the PSF parameters along the major and minor axes and used the

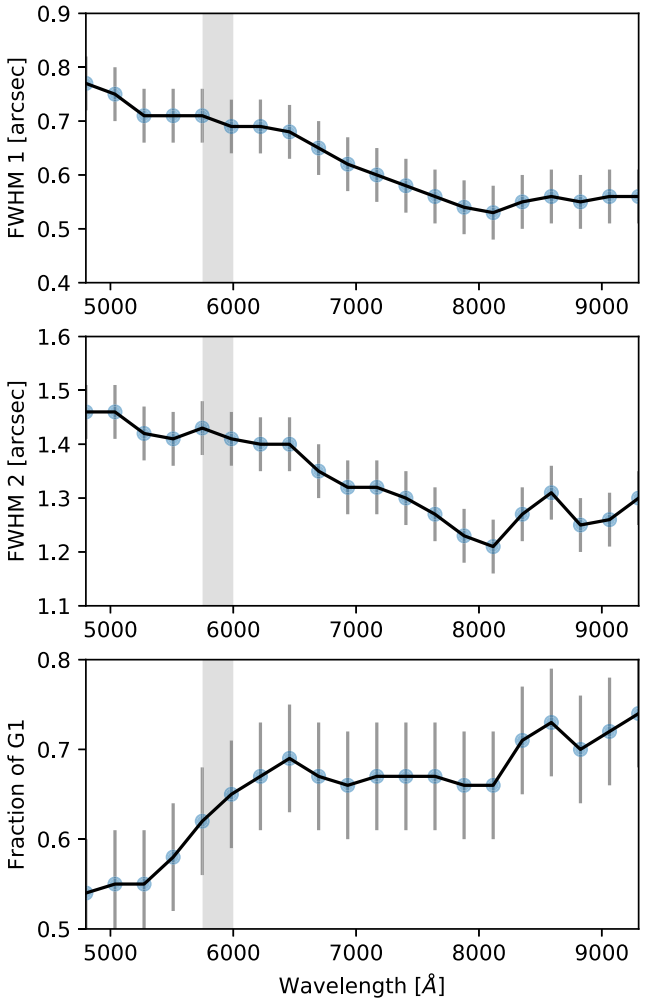

Figure 3. Parametrization of the AO-assisted MUSE PSF as a function of wavelength. FWHM of the two Gaussian components and the fraction of the narrow Gaussian (G1) were derived from the PSF star fit. The two Gaussians were fitted for each wavelength bin (width of 500 Å) between 4800 and 9300 Å. The grey shaded area indicates the wavelength range in which the laser guide star light is blocked by the NaD notch filter.

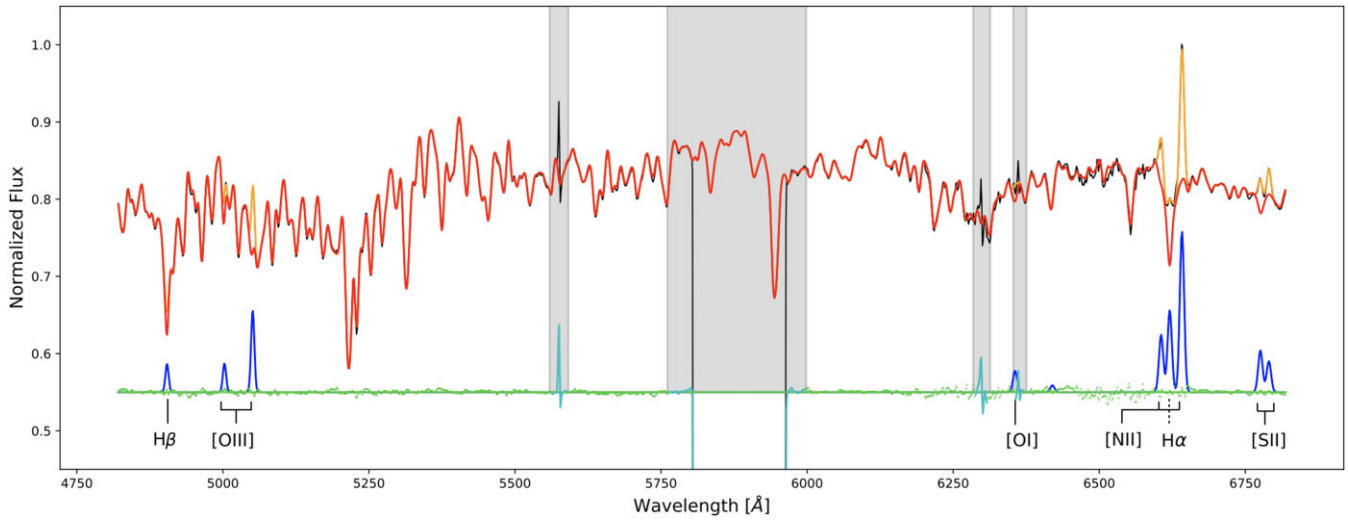

Figure 4. Integrated MUSE spectrum at observed wavelength and best-fitting PPXF fit of NGC 6958 displayed in the MILES spectral range. The integrated spectrum (black solid line) was obtained by summing up all spectra of the IFU data cube within a radius of 15 arcsec. This integrated spectrum was fitted using the PPXF routine in order to derive an optimal stellar template (red line). We simultaneously fitted the emission lines (blue) and the fit composed of gas and stellar continuum is shown in orange. The fitting residuals between spectrum and best-fitting model are shown as green dots and are shifted up by 0.55. Regions that were masked in the fit, owing to either the AO NaD notch filter or insufficient sky correction, are indicated as grey shaded regions.

differences as uncertainties. The spatial resolution clearly improves when going from the blue to the red end of the MUSE data by about 35 per cent. We noticed a deterioration in the quality of the PSF at around 8000 Å that likely resulted from incomplete skyline removal in that region. All of our measurements are in agreement with the study of the MUSE PSF by Fusco et al. (2020) if we assume a poor natural seeing of about 1.2, as recorded in the raw data, and translate our Gaussian measurements into MOFFAT parametrization. Being taken in mediocre weather conditions, our data set does not reach the expected resolution that could be obtained with full AO-assisted MUSE observations (e.g. Knapen, Comerón & Seidel 2019), but is still a significant improvement over what would have been achieved in these conditions without AO. Owing to the strong priors on the broad Gaussian when estimating the PSF in the galaxy nucleus, we used the PSF values from the PSF star in the dynamical modelling of NGC 6958 (Section 4).

3.2 Kinematics extraction

We used the PYTHON implementation of the penalized Pixel Fitting method[3] (PPXF; Cappellari & Emsellem 2004; Cappellari 2017) to measure the line-of-sight velocity distribution (LOSVD) of each Voronoi bin of the MUSE data. PPXF fits the observed galaxy spectrum by convolving a linear combination of stellar templates with the best-fitting LOSVD. The stellar templates were taken from the medium-resolution Isaac Newton Telescope Library of Empirical Spectra (MILES; Sánchez-Blázquez et al. 2006; Falcón-Barroso et al. 2011) stellar library (version 9.1). We used the full MILES library consisting of 985 stars and fitted the integrated MUSE spectrum to derive an optimal template. As the MILES templates have a similar spectral resolution to the MUSE spectra,[4] we did not need to degrade either of the two data sets. MILES stellar templates span the wavelength range of 4760–7400 Å and were fitted to the wavelength range from 4820 to 6820 Å in the galaxy spectrum. We chose this wavelength range in the galaxy spectrum as we noticed an increased template mismatch at wavelengths redder than 7000 Å. The region between 5750 and 6000 Å was blocked in the observation to avoid contamination and saturation of the detector by the strong sodium laser light. During the PPXF fit, we masked the blocked region and insufficiently removed skylines. We performed two runs: In one run, we parametrized the LOSVD as a simple Gaussian (V, σ) and used the kinematics for the JAM (Jeans anisotropic modelling) modelling (Section 4.3). In the second run, we parametrized the LOSVD as Gauss–Hermite polynomial of the order of 6 regulated by a bias of 0.8. We used the second set of extracted kinematics in the Schwarzschild modelling (Section 4.2). The stellar continuum was modelled with a seventh-order additive Legendre polynomial.

The residuals from the stellar fit showed a richness of emission-line features (see Fig. 4), such that we decided to fit for the emission lines and the stellar continuum simultaneously. We were thus able to detect and measure the H α λ6563 and H β λ4861 Balmer lines and the [O III] $\lambda\lambda$4959, 5007, [O I] $\lambda\lambda$6364, 6300, [N II] $\lambda\lambda$6548, 6583, and [S II] $\lambda\lambda$6716, 6731 forbidden line doublets over the whole MUSE FoV. We first derived a best-fitting optimal template to the integrated spectrum of the full MUSE FoV (see Fig. 4). After having found the optimal template (using both stellar continuum and gas emission information), we reran PPXF on the individual spectra of each bin of the MUSE observations and used the global-spectrum optimal template to extract the stellar and ionized-gas kinematics simultaneously. During the fit, we treated the stars and different gas elements as separate components and assigned individual LOSVD to each of them. We made sure that doublets were treated as one gas component with a single value for V and σ. We then estimated the uncertainties using Monte Carlo simulations (with 500 realizations)

[3] https://pypi.org/project/ppxf/

[4] Note that the MUSE LSF is not uniform over the complete wavelength range. We have analysed the effect of the non-uniformity on the extracted kinematics in Thater et al. (2019). By not convolving the MILES spectra adaptively to the spectral resolution of MUSE, we impose a systematic uncertainty of about 3 km s^{-1} in the velocity dispersion that we took into account in the dynamical modelling.

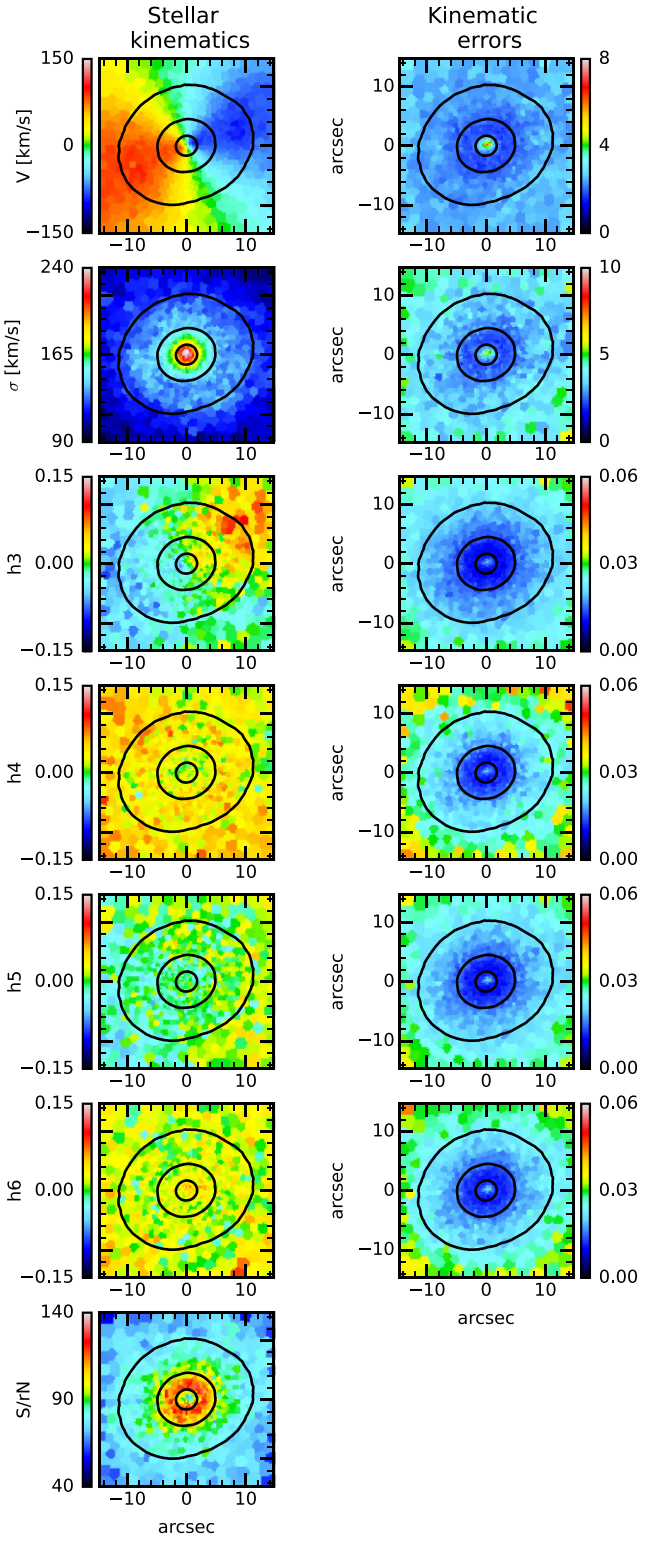

Figure 5. MUSE stellar kinematic maps (left) and kinematic errors (right) extracted from our full-spectrum fit. From top to bottom, the panels show maps of S/rN, mean velocity (V), velocity dispersion (σ), and the Gauss–Hermite moments h_3, h_4, h_5, and h_6. The black contours indicate the isophotes from the collapsed data cube. North is up and east is to the left.

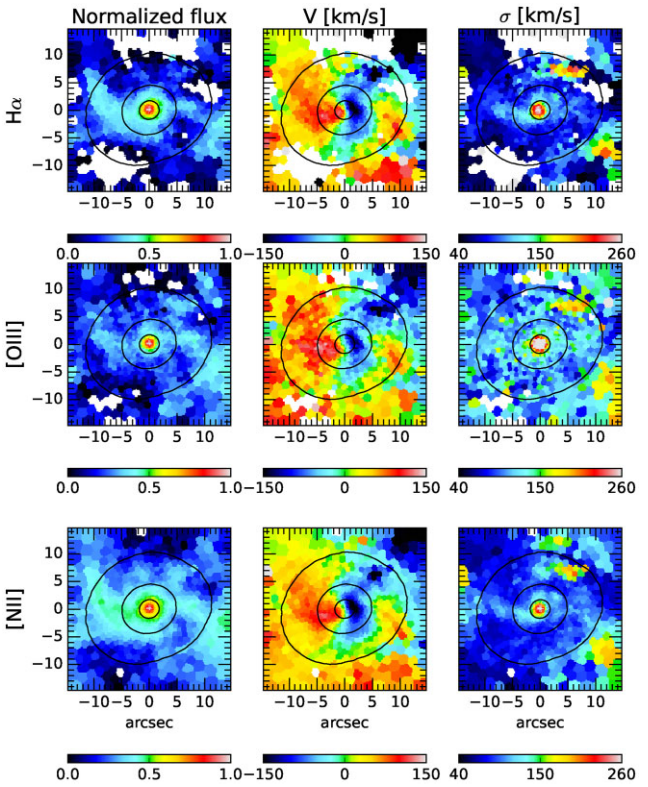

Figure 6. MUSE ionized-gas kinematics derived from the simultaneous fit of stellar continuum and emission lines. The panels show the ionized-gas distribution in log scale, mean velocity (km s^{-1}), and velocity dispersion (km s^{-1}) maps traced by H α, [O III], and [N II]. The maps were masked at a line significance A/rN below 3. North is up and east is to the left.

on each Voronoi bin as described in Thater et al. (2019). We therefore used the standard deviation of the residuals between the galaxy spectrum and the best-fitting PPXF model to define a residual noise (rN) for each Voronoi bin. The signal-to-residual noise (S/rN) measures then not only the quality of the data but also the quality of the spectral fit. Due to the high S/rN of the observations (see Fig. 5), we obtained very small stellar kinematic errors of typically 2.5 km s^{-1} for the mean velocity, 4 km s^{-1} for the velocity dispersion, and 0.02, 0.03, 0.02, and 0.02 for the higher order Gauss–Hermite moments. The errors of the ionized gas kinematics from the Monte Carlo simulations reached typical values of 4–8 km s^{-1} for the mean velocity and 5–9 km s^{-1} for the velocity dispersion. We also noticed a decrease of the S/rN for $R < 2$ arcsec that led to increased errors in this region. The lower S/rN is caused by the nuclear dust disc and we discuss its effect on our $M_{\rm BH}$ measurement in Section 4.4.1.

We show our extracted stellar kinematics maps in Fig. 5 and the kinematic maps of the ionized gas in Fig. 6. As expected from the selection criteria for this galaxy, the extracted stellar kinematics features of NGC 6958 are very smooth and do not show any substantial irregularities in the central 15 arcsec. After subtracting the systemic velocity of 2630 km s^{-1}, the rotational velocities reach up to 130 km s^{-1}, and a clear velocity dispersion peak is visible reaching up to 250 km s^{-1}. The h_3 moment also shows the clear anticorrelation to the mean velocity, and the h_4 moment increases

slightly asymmetrically with increasing radius. Similar features are also seen within the higher moments, albeit they do not strongly differ from 0. All in all, NGC 6958 has very regular stellar kinematics at radii <15 arcsec and is therefore ideally suited for the tests that we want to perform in this study. The extracted emission-line maps show a different picture to the stellar kinematic maps. For each of the three rows in Fig. 6, we present the ionized-gas distribution, the mean velocity, and the velocity dispersion of the LOSVD. Based on the arguments in Sarzi et al. (2006), we decided our emission line fits to be unreliable for amplitude-to-residual-noise ratios (A/rN) < 3 and in Fig. 6 for each emission-line map masked the bins at lower A/rN (where rN was measured from the rN of the PPXF fit). The morphology of the ionized-gas distribution and kinematics are very similar between the different emission lines but differ strongly from the stellar kinematics maps. The gas rotates at faster velocities, but has a similar velocity dispersion in the galaxy centre. It is notable that, while the ionized gas shows regular features in the central 5 arcsec, outside of this region, we see very irregular structures largely dominated by receding motion. The irregular motion of the gas could be due to its recent acquisition (Malin & Carter 1983; Saraiva et al. 1999), but we will postpone this analysis to the follow-up publication. We will also investigate in the follow-up publication, whether it will be possible to derive the black hole mass from the ionized gas to have a comparison of the effects of cold versus warm gas tracers. For now, we will focus on the stellar-based dynamical model, described in the next section.

4 DYNAMICAL MODELLING

We modelled the stellar kinematics of NGC 6958 using the two independent methods: axisymmetric Schwarzschild modelling and JAM. Both methods are commonly used for $M_{\rm BH}$ determinations and a cross-comparison of the respective results can serve as check on the robustness of the measurement (e.g. Ahn et al. 2018; Krajnović et al. 2018; Thater et al. 2019; den Brok et al. 2021). We refer to Thater et al. (2017, 2019) for a detailed description of the methods and repeat here just the main assumptions and parameters used in our models.

4.1 Mass model

Constructing dynamical models and deriving black hole masses require an estimate of the gravitational potential of the galaxy. We inferred the stellar potential directly from the luminosity of the galaxy multiplied with its (radially varying) M/L. For a precise model of the stellar luminosity, a combination of high-resolution *HST* and deep large-scale imaging data is essential.

We used the Multi-Gaussian Expansion (MGE; Cappellari 2002) fitting routine[5] to parametrize the surface brightness of NGC 6958 with a sum of two-dimensional Gaussians. We simultaneously fitted the sky-subtracted NICMOS and the WFC3 images; within a radius of 7 arcsec, the light distribution was constrained with the high-resolution NICMOS image and for larger radii with the WFC3 image. We matched the surface brightness profiles of the two data sets by re-scaling the WFC3 imaging data to the central NICMOS light profiles and used the NICMOS imaging for the photometric calibration. During the fit, we took the NICMOS PSF into account to obtain the intrinsic light distribution of the galaxy. This is a crucial step as the accuracy of our black hole mass measurement depends on how well we can describe the stellar mass in the centre of the galaxy. We generated the NICMOS PSF using the TinyTim PSF modelling tool (Krist & Hook 2001) and parametrized the PSF as a sum of Gaussians. Fig. 7 shows our best-fitting MGE model overplotted on the observed surface brightness distribution of NGC 6958. While the central parts of the *HST* image are well fitted with the MGE model, we noticed a clear isophote twist by almost 30 deg at $R > 15$ arcsec. Our dynamical models do not account for isophotal twists as they assume axisymmetry. However, the centre probed by our stellar kinematics shows no significant isophotal twist and relaxed stellar kinematics (see Fig. 5). We therefore kept the position angle constant while fitting the surface brightness. The profile of our final MGE is shown in Fig. S1 of the supplementary material. Our final MGE consists of 10 concentric Gaussian components. We converted the flux units into physical units of $L_\odot$ pc^{-2} following the guideline and zero-point given by Thatte (2009). For the conversion, we adopted a value of 4.64 mag (Willmer 2018) for the absolute AB magnitude of the sun in the *H* band. We also took the Galactic extinction of $A_{\rm F160} = 0.026$ mag (Schlafly &

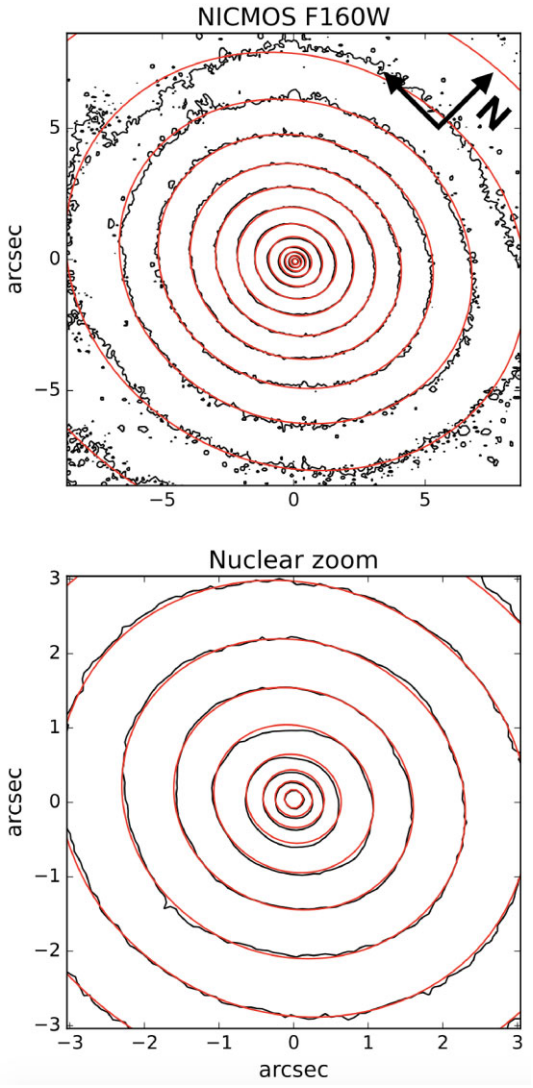

Figure 7. Isophotes of the NICMOS image of NGC 6958 within an FoV of 20 arcsec × 20 arcsec (top) and a cut-out of the central 6 arcsec × 6 arcsec (bottom). The contours of our best-fitting MGE model (red) are superimposed on the *HST* images (black).

[5]https://pypi.org/project/mgefit/

Table 3. *HST*/NICMOS F160W + *HST*/WFC3 F160W MGE model.

j	$\log(I_j)$ ($L_{\odot,H}$ pc^{-2})	σ_j (arcsec)	q_j	$\log(M_j^{const})$ ($M_\odot$)	$\log(M_j^{var})$ ($M_\odot$)
(1)	(2)	(3)	(4)	(5)	(6)
1	5.751	0.053	0.91	8.373	8.462
2	5.131	0.207	0.91	8.941	9.028
3	4.562	0.292	0.91	8.669	8.754
4	4.57	0.704	0.87	9.424	9.504
5	4.252	1.52	0.89	9.785	9.856
6	3.903	3.04	0.89	10.036	10.09
7	3.145	6.728	0.85	9.946	9.968
8	2.88	13.311	0.84	10.269	10.261
9	2.164	31.543	0.82	10.294	10.277
10	1.443	65.187	0.89	10.239	10.221

Notes. Column 1: Index of the Gaussian component. Column 2: Surface brightness. Column 3: Projected Gaussian width along the major axis. Column 4: Projected axial ratio for each Gaussian component. Columns 5 and 6: Total mass of Gaussian component. In column (5), the constant dynamical M/L = 0.91 $M_\odot/L_{\odot,H}$ from the Schwarzschild modelling (Section 4.2) was used to determine the mass of each Gaussian component and in column (6) the radially varying stellar M/L from Section 4.4.3 was used. The model has a uniform position angle of 110.8° for all Gaussian components.

Finkbeiner 2011) into account. The converted MGE parameters are shown in Table 3 and describe the luminosity of NGC 6958.

The two-dimensional light parametrization is then (assuming an axisymmetric potential and the inclination of the galaxy) deprojected into three-dimensional space. Multiplied with the (radially varying) M/L in the given band, we thus obtained a model of the mass density from which the gravitational potential can be calculated via the Poisson equation.

We also used our MGE model to derive the effective radius of the galaxy. We followed the approach described in Cappellari et al. (2013) and used the routine `mge_half_light_isophote` of the PYTHON JAM package described in Section 4.3. The derived effective radius is 15.″3 that translates into 2.59 kpc at a distance of 35 Mpc.

4.2 Axisymmetric Schwarzschild models

In this first approach, we modelled the collective motion of stars within an FoV of 30 arcsec × 30 arcsec using the axisymmetric Schwarzschild (1979) orbit superposition modelling method, with the software implementation described in Cappellari et al. (2006). In this method, we calculated the predictions for the Gauss–Hermite polynomials up to h_6 and compared them with the observed stellar kinematics. For velocity, velocity dispersion, h_3, and h_4, we used the measured kinematic errors, while for h_5 and h_6 we set the errors to a constant 0.15 to account for systematics in the kinematic extraction and reduce their influence on the χ^2 distribution. We also bi-symmetrized the MUSE kinematics along $PA_{kin} = 109°$ as the models are bi-symmetric by construction. PA_{kin} was derived from the MUSE velocity field within a radius of 5 arcsec using the routine `fit_kinematic_pa`[6] (Krajnović et al. 2006). The Schwarzschild models were computed as described in Thater et al. (2019) by running a grid of models of the two free parameters (M_{BH} and M/L).

Axisymmetric Schwarzschild models become highly degenerate at low inclinations, so we adopt a fixed $i = 45°$, which is the inclination of the nuclear gas disc that likely lies in the galaxy mid-plane (Thater et al., in preparation). We need to use the inclination of the gas disc as it is not possible to constrain the inclination of the galaxy with axisymmetric Schwarzschild models (Krajnović et al. 2005; Lipka & Thomas 2021). However, in Section 4.4.2, we discuss how the results will change for a more edge-on ($i = 90°$) model. We also took the spatial PSF and binning of the kinematics into account, before comparing the Schwarzschid models to the observations. For our orbit library, we sampled the orbits via 41 logarithmically spaced orbit energies, 11 linearly spaced orbit angular momenta L_z, and 11 linearly spaced non-classical third integral values *I3*. In order to improve the smoothness of the model, each orbit was split into 6^3 suborbits with similar initial conditions. Additional smoothing was applied by setting a moderate regularization of 4 (van der Marel et al. 1998).

We ran a first coarse grid along $(M_{BH}/M_\odot) \in [10^6, 5 \times 10^9]$ and $(ML^{-1}/M_\odot\ L_{\odot,H}^{-1}) \in [0.1, 3.0]$ to get an indication of the global minimum of the χ^2 distribution. Then, we centred a refined grid on that global χ^2 minimum with 20 M_{BH} and 16 M/L sampling locations. Fig. 8 shows our final grid of Schwarzschild models for NGC 6958 with overplotted χ^2 contours. From the χ^2 distribution, we derived the best-fitting parameters to be $M_{BH} = (3.6^{+2.5}_{-1.3}) \times 10^8\ M_\odot$ and $M/L = 0.91 \pm 0.04\ M_\odot/L_{\odot,H}$ within 3σ significance ($\Delta\chi^2 = 11.8$). Our data revealed a single high-velocity dispersion pixel at 257 km s^{-1} that can be fitted well by a model with $M_{BH} = 4.7 \times 10^8\ M_\odot$ and $M/L = 0.91\ M_\odot/L_{\odot,H}$. However, this Schwarzschild model has too high velocity dispersion in the surrounding pixels and therefore a considerably higher χ^2. As this plausible higher mass is included in the 3σ uncertainties of our measurement, we decided for $3.6 \times 10^8\ M_\odot$ as final result of our Schwarzschild models. Such a black hole has an SoI (sphere of influence) of 57 parsec that corresponds to 0.″34 at a distance of 35 Mpc.

The grid in Fig. 8 also indicates the formally lowest black hole mass detectable with the spatial resolution of our MUSE observations (blue dashed line). While properly spatially resolving the SoI was perceived to be a strict condition for the robustness of black hole mass estimates for a long time (see e.g. discussion by Kormendy & Ho 2013), Krajnović et al. (2009) and Thater et al. (2019) have shown that when using high-quality IFU data and the sophisticated Schwarzschild modelling method, it is still possible to constrain the black hole mass, albeit with more care required around possible systematics and larger final error budgets (e.g. Rusli et al. 2013). Fig. 8 implies that we can measure a black hole mass that is half of the nominally minimal detectable black hole mass of $\sim 6 \times 10^8\ M_\odot$. The robustness of our measurement is illustrated by the $V_{rms} = \sqrt{V^2 + \sigma^2}$ maps in Fig. 8, given that the model V_{rms} of the too low and too high black hole masses significantly deviate from the observed V_{rms}. A comparison of the remaining kinematic moments for the best-fitting Schwarzschild model and the observation is also shown in Figs S2 and S3 of the supplementary material.

4.3 Jeans anisotropic models

We used the axisymmetric JAM method[7] (Cappellari 2008, 2020) to obtain a second independent M_{BH}. Assuming an axisymmetric galaxy shape, JAM predicts the average second velocity moment along the LOS $\langle V_{los}^2 \rangle^{1/2}$. The model $\langle V_{los}^2 \rangle^{1/2}$ is then compared to the observed V_{rms} of NGC 6958 (taking the spatial PSF into account). The modelling depends on the black hole mass M_{BH}, the M/L, and the anisotropy parameter that describes the flattening of the velocity ellipsoid along the minor axis. In JAM, the alignment of the velocity

[6] https://pypi.org/project/pafit/

[7] We used the jam_axi_proj.py routine, version 6.3.1 of the JAMPY PYTHON software package that is downloadable at https://pypi.org/project/jampy/.

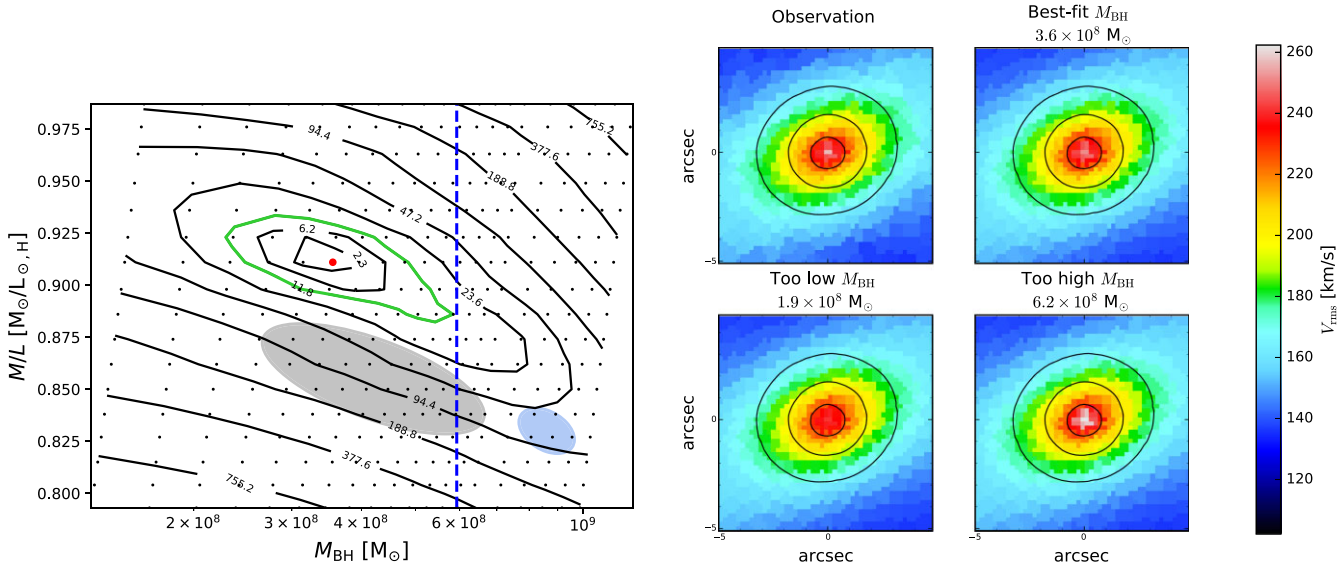

Figure 8. Results of the axisymmetric Schwarzschild modelling. Left-hand panel: Grid of our Schwarzschild models (indicated as black dots) over various M/Ls and black hole masses. The overplotted contours indicate the $\Delta\chi^2 = \chi^2 - \chi^2_{\rm min}$ levels, the green contour indicating the 3σ confidence interval. The best-fitting model was derived as the minimum of the χ^2 distribution and is shown as red dot. The grey and blue shaded areas indicate the 3σ confidence intervals for $M_{\rm BH}$ and M/L that we have estimated using $\rm JAM_{sph}$ and $\rm JAM_{cyl}$, respectively (Section 4.3). Note that the M/L from Schwarzschild is larger than that from JAM. This is due to a radial dynamical M/L gradient as explained in Section 4.3. The dashed blue line indicates the smallest black hole mass that we expect to robustly detect based on the SoI argument and the achieved resolution. Right-hand panel: Visual comparison between the symmetrized observed $V_{\rm rms}$ map, the $V_{\rm rms}$ map of the model with best best-fitting model parameters, and a too high and a too low black hole mass at fixed best-fitting M/L. The black contours indicate the observed light distribution of the galaxy. North is up and east is to the left.

ellipsoid can be chosen to be cylindrical or spherical. We used both extreme configurations to test the robustness of our models and call them 'cyl' and 'sph'. The definition of the anisotropy parameter depends on the alignment of the velocity ellipsoid: $\beta_z^{\rm cyl}(R, z) = 1 - (\langle v_z\rangle/\langle v_R\rangle)^2$ versus $\beta^{\rm sph}(r, \theta) = 1 - (\langle v_\theta\rangle/\langle v_r\rangle)^2$.

Because of the low inclination of NGC 6958, we did not keep the inclination as a free parameter. Instead, we set it to 45° derived from the molecular gas analysis (same inclination as for the Schwarzschild models). Compared to the Schwarzschild method discussed earlier, our JAM models are fitted to the central 10 arcsec × 10 arcsec of the stellar kinematics parametrized by a pure Gaussian (without Hermite moments). The 10 arcsec FoV was chosen to balance the weight of the very central kinematics that are affected by the dynamical potential of the black hole and the use of more extended kinematics to reduce the $M_{\rm BH}$–M/L degeneracy.

We derived the best-fitting JAM model using a Bayesian framework as implemented in EMCEE (Foreman-Mackey et al. 2013) as described in Thater et al. (2019). 200 walkers explored the parameter space within the burn-in phase (500 steps) and were tracked during the post-burn-in phase (500 steps) to generate posterior distributions. The parameter space was defined by uniform priors in the ranges: $\log(M_{\rm BH}/{\rm M}_\odot) \in [4.8, 9.8]$, $\beta \in [-1, +1]$, and $(ML^{-1}/{\rm M}_\odot\ {\rm L}^{-1}_{\odot,{\rm H}}) \in [0.1, 20]$. To derive robust results, we carefully ensured that our Markov chain Monte Carlo (MCMC) chain converged by visually checking the burn-in plots and running several Markov chains. We obtained the best-fitting parameters within 99.7 per cent confidence level (which is in accordance with 3σ in a normal distribution) from the posterior distributions. We fitted JAM models using the formal kinematic uncertainties derived in Section 3.2, but the χ^2 of these models was dominated by the fit to the many bins at large radii rather than by the kinematics inside the black hole SoI. For this reason, the fit was driven by the inaccuracies of the modelling assumptions (e.g. constant anisotropy) rather than the black hole mass and failed to reproduce the kinematics in the black hole SoI within the formal errors. These fits gave too large $M_{\rm BH}$ and correspondingly too large central $V_{\rm rms}$ values.

To be able to interpret the $M_{\rm BH}$ returned by JAM, it is essential for the models to fit the kinematics within the uncertainties inside the SoI, where the effect of the SMBH dominates. To achieve this, we used a heuristic approach to deal with systematic uncertainties proposed by van den Bosch & van de Ven (2009). It consists of expanding the confidence level on χ^2 by an amount equal to its variance. When using a Bayesian approach, this same result is achieved by multiplying the kinematic errors by $(2N)^{1/4}$, where N is the number of constraints, as shown in Mitzkus, Cappellari & Walcher (2017). A similar approach was also applied by Drehmer et al. (2015) to improve the JAM fit of their central $V_{\rm rms}$. However, here we differ from previous works by keeping unchanged the kinematic uncertainties inside the approximate black hole SoI ($R < 0\farcs5$), while only increasing the uncertainties at larger radii. This ensures that we have a proper scaling of the $M_{\rm BH}$ errors and additionally makes sure that the fit is maximally sensitive to the black hole's kinematic influence while still matching the kinematics at larger radii.

Our model with modified kinematic errors resulted in $M_{\rm BH} = (8.6^{+0.8}_{-0.8}) \times 10^8\ {\rm M}_\odot$, $\beta_z^{\rm cyl}$ of -0.02 ± 0.06, and a dynamical M/L of $0.83 \pm 0.02\ {\rm M}_\odot/{\rm L}_{\odot,{\rm H}}$ for $\rm JAM_{cyl}$. On the other hand, $\rm JAM_{sph}$ gave a significantly lower $M_{\rm BH} = (4.6^{+2.5}_{-2.7}) \times 10^8\ {\rm M}_\odot$, $\beta^{\rm sph}$ of 0.38 ± 0.17, and a dynamical M/L of $0.86 \pm 0.02\ {\rm M}_\odot/{\rm L}_{\odot,{\rm H}}$. The final posterior distributions of our JAM models are shown in Fig. C1. The cuts of the best-fitting JAM models (Fig. 9) show that our models with modified uncertainties for larger radii reproduce the central kinematics very well. The $M_{\rm BH}$ measurement from JAM is larger than the mass measurement from the Schwarzschild models and only the black hole mass from $\rm JAM_{sph}$ is (within 3σ) consistent with the one derived with Schwarzschild. Also, the M/L measured with both JAM implementations is lower than that with the Schwarzschild models.

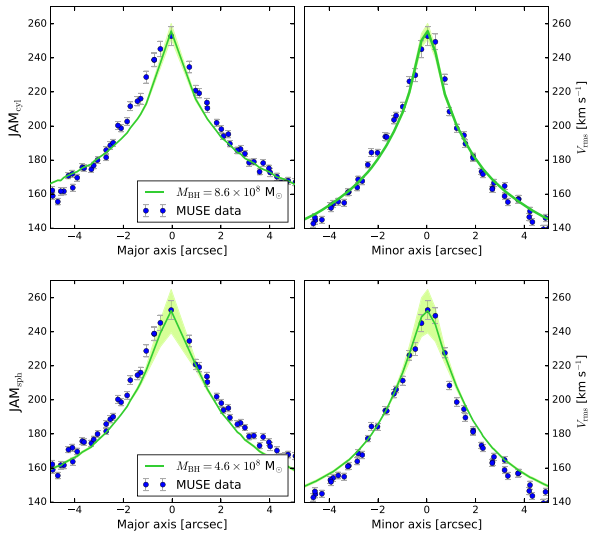

Figure 9. Results of the JAM modelling with cylindrical (JAM_{cyl}) and spherical (JAM_{sph}) velocity ellipsoid alignment. The panels show cuts of the observed $V_{rms} = \sqrt{V^2 + \sigma^2}$ (blue dots) along the and minor axis of NGC 6958. Overplotted are the V_{rms} of the best-fitting JAM models (solid green) and models that are within the M_{BH} uncertainty range from our MCMCs (green shaded area).

Table 4. Results of the different M_{BH} measurement methods – fiducial models with constant (top) and radially varying (bottom) M/L.

Method	FoV (arcsec)	M_{BH} ($\times 10^8$ $M_\odot$)	M/L ($M_\odot/L_{\odot,H}$)	χ^2/d.o.f.
(1)	(2)	(3)	(4)	(5)
Schwarzschild	30	$3.6^{+2.5}_{-1.3}$	0.91 ± 0.04	0.86
JAM_{cyl}	10	$8.6^{+0.8}_{-0.8}$	0.83 ± 0.02	0.24
JAM_{sph}	10	$4.6^{+2.5}_{-2.7}$	0.86 ± 0.02	0.21
Schwarzschild	30	$2.9^{+2.2}_{-1.8}$	0.87 ± 0.04	0.87
JAM_{cyl}	10	$7.3^{+1.2}_{-1.1}$	0.80 ± 0.02	0.20
JAM_{sph}	10	$4.1^{+2.2}_{-1.8}$	0.82 ± 0.02	0.18

Notes. Column 1: M_{BH} measurement method using an inclination of 45°. Column 2: FoV of the data used in the methods. Columns 3, 4, and 5: Parameters of the best-fitting models [black hole mass M_{BH}, M/L, and the χ^2 over the degree of freedoms (using the modified kinematic uncertainties derived in Section 4.3)]Is it possible to add a vertical line after the 4th column? This line would significantly improve the understanding of this table.

It is important to note that we fit the Schwarzschild models to the full MUSE kinematics, while we fit the JAM models only to the nuclear kinematics. For this reason, given that we assume mass-follow-light models in both cases, this M/L difference suggests that the M/L increases with radius. A possible reason for this increase could be the dark matter, which we ignored here, but which may start affecting the total density slope at the largest radii probed by the MUSE data. We demonstrate the correctness of this interpretation in Section 4.4.5.

4.4 Systematic uncertainties of the measurement

We summarize the main results of the Schwarzschild and JAM models in Table 4 and from now on refer to them as fiducial models. In the following section, we show several tests for systematics that should be considered when deriving robust black hole mass measurements. The following sections are ordered such that we first look for systematics in the stellar kinematics data, then systematics from the dynamical model assumptions and finally systematics arising from the mass model of the galaxy. The tests have a similar effect on both the Schwarzschild and JAM models. In order to keep the section on systematics clear, we explain the results of the Schwarzschild models in the main text and provide the results for the two JAM implementations in Table C1.

4.4.1 *Systematics in the stellar kinematics extraction*

Applying radially dependent kinematic errors: We noticed that within a radius of 2 arcsec from the centre of NGC 6958, our MUSE kinematic maps showed relatively low S/rN (≈70) compared to further out (≈100), leading to elevated kinematic errors in this region. For detailed maps, see Fig. S5 of the supplementary material. We carefully inspected the fitting of this region by masking and de-masking the spectrum but could not improve the S/rN significantly. As the low-S/rN region can also be seen in the blue range of the fit but disappears in the redder CaT region (next subsections), we believe that the higher S/rN originates from the about 4 arcsec in diameter extended nuclear dust disc. The accuracy of the black hole mass measurement is strongly driven by these central pixels. We therefore carried out a Schwarzschild modelling test in which we applied radially increasing kinematic errors: $(V_{err}/\mathrm{km\ s^{-1}}) = 3.5 + 0.5 \times (R/\mathrm{arcsec})$ and $(\sigma_{err}/\mathrm{km\ s^{-1}}) = 4.0 + 0.5 \times (R/\mathrm{arcsec})$. This change reduced the velocity errors from 4.9 to 3.5 km s^{-1} (at $R = 0$ arcsec) and increased from 2.5 to 6.0 km s^{-1} (at $R = 5$ arcsec), and for the velocity dispersion errors from 5.0 to 4.0 km s^{-1} (at $R = 0$ arcsec) and 2.2 to 6.5 km s^{-1} (at $R = 5$ arcsec). This procedure is similar to applying higher weights to the central region of the kinematics during the dynamical modelling, but is a strong modification of the data set and therefore should only serve as a test for the accuracy of the measurement. Schwarzschild models using modified central kinematic errors have the following best-fitting parameters: $M_{BH} = (4.4^{+1.8}_{-1.9}) \times 10^8$ $M_\odot$ and $M/L = 0.88 \pm 0.04\,M_\odot/L_{\odot,H}$. The derived M_{BH} is slightly higher than the fiducial, but consistent with the results presented in Section 4.2.

Exclusion of emission lines in the kinematics fit: Looking at Fig. 4, it is evident that NGC 6958 shows a richness of ionized gas emission lines in its central region. While we have simultaneously fitted the emission lines and the stellar continuum in Section 3.2, it is also common practice to mask the emission lines during the spectral fit. In this test, we extracted stellar kinematics maps by keeping the same spectral coverage but masking the emission lines. The resulting kinematics are very similar to the kinematics extracted with fitting the gas emission lines and deviations are within the very small kinematics errors (see Fig. 10). Running Schwarzschild models on this different set of kinematics, the best-fitting model parameters are: $M_{BH} = (3.6^{+1.7}_{-1.3}) \times 10^8$ $M_\odot$ and $M/L = 0.91 \pm 0.04$ $M_\odot/L_{\odot,H}$, which is very close to our main result from the Schwarzschild modelling. While the exclusion of the emission lines during the PPXF kinematics extraction provided a slightly better S/rN, there is no change to the results of this paper when including them.

Fitting only the blue spectral range of MUSE: While extracting the stellar kinematics, we noticed a larger discrepancy between observed spectrum and PPXF fit in the red wavelength range (around 6500 Å) than in the blue (see Fig. 4). We therefore tested the robustness of our result by only fitting the spectral region between 4820 and 5750 Å. Doing so, the median S/rN increased

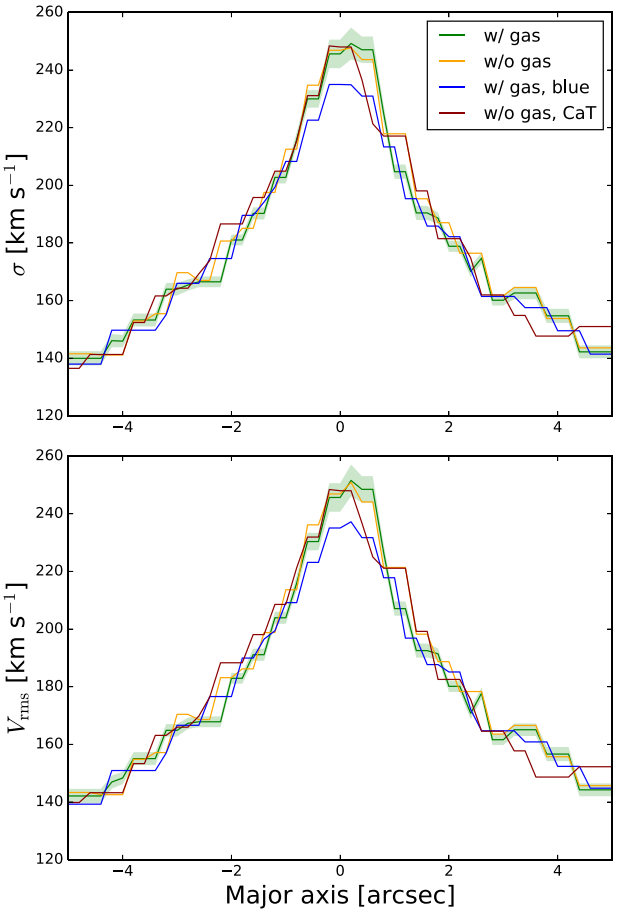

Figure 10. Comparison between the different stellar kinematics extractions with PPXF . Shown are the derived velocity dispersion (top panel) and the $V_{\rm rms}$ (bottom panel) of the extraction including gas emission lines (green), without including gas emission lines (orange), fitting the blue part of the spectrum with emission lines (blue), and fitting the calcium triplet (red). We also show the kinematic errors for the extraction including gas emission lines as green shaded area. Except for that of the blue part of the spectrum, the extractions are consistent within their uncertainties within the central region.

from 104 to 114. We created Schwarzschild models using the same inputs as with the fiducial model but replacing the stellar kinematic maps and the corresponding PSF (see Table 2). The best-fitting parameters are: $M_{\rm BH} = (3.1^{+2.2}_{-1.9}) \times 10^8$ M$_\odot$ and a dynamical M/L of 0.84 ± 0.04 M$_\odot$/L$_{\odot,\rm H}$. As expected from the lower central $V_{\rm rms}$ (Fig. 10), the obtained black hole mass was lower in this case than that for the other three kinematic extractions but consistent within 1σ of the measurement uncertainty. While we do not exactly know the reason for the lower central $V_{\rm rms}$, there are two possibilities. Either our spectral library is not fully representative for the bluer stars in this spectral range or the dust is hiding the strongly accelerated stars close to the black hole (as this difference is mostly seen in the central 2 arcsec), leading to an underestimated black hole mass. Hence, we strongly advise against only using the blue spectral region of MUSE if there is any indication of nuclear dust in the galaxy.

Fitting only CaT: MUSE offers not only a wide FoV, but also has the great advantage of providing high-quality spectra over a wide wavelength range, including also characteristic features like the Ca II triplet around 8500 Å. The Ca II triplet can be used to obtain a black hole mass measurement at a moderately higher spatial resolution of 0.″56 instead of 0.″69 (see Table 2) and in a wavelength regime less affected by dust. We therefore also derived kinematic maps from this spectral feature by only fitting the wavelength range between 8500 and 8800 Å. For this PPXF fit, we used the 61 stars from the Phoenix synthetic stellar library (Husser et al. 2013), which covers the spectral range from 8350 to 9020 Å at a resolution of 1.0 Å. We made sure to degrade those template spectra to match the instrumental resolution of our MUSE data before starting the fitting procedure. Schwarzschild models using the Ca II triplet kinematics, uncertainties, and PSF as input (while keeping the remaining inputs the same) yield the best-fitting parameters: $M_{\rm BH} = (3.5^{+2.7}_{-2.0}) \times 10^8$ M$_\odot$ and a dynamical M/L of 0.95 ± 0.05 M$_\odot$/L$_{\odot,\rm H}$. The black hole mass measurement is very consistent with the measurements using the optical wavelength range shown in Fig. 4. Due to the consistency, this test serves as confirmation that the circumnuclear dust disc is not significantly affecting the stellar kinematics extraction.

4.4.2 *Systematics in the dynamical modelling*

Symmetrization in Schwarzschild models: All of our dynamical models are by construction, axisymmetric. However, how to deal with this assumption is handled differently in Schwarzschild and JAM models. While the unmodified extracted kinematics are fitted with JAM, in Schwarzschild models the kinematics are usually symmetrized before the dynamical modelling to constrain the freedom of the models better and reduce the noise of the observations (Krajnović et al. 2005; van den Bosch & de Zeeuw 2010). We therefore also ran a Schwarzschild model with unmodified kinematics. This run resulted in wider χ^2 contours than by bi-symmetrizing the kinematics. However, the resulting black hole mass does not differ significantly: The best-fitting black hole mass using the unmodified kinematics is $M_{\rm BH} = (4.0^{+2.3}_{-1.7}) \times 10^8$ M$_\odot$ and M/L of 0.88 ± 0.05 M$_\odot$/L$_{\odot,\rm H}$. Hence, the symmetrization of the kinematics does not affect our main result. A similar result was also found in Walsh et al. (2012) when switching on the symmetrization for their measurement.

Inclination: When creating the dynamical models, we assumed a galaxy inclination of 45° based on the estimated inclination of the nuclear molecular gas disc (Thater et al., in preparation). However, the inclination plays a significant role in the deprojection of the luminosity model and can therefore bias the final results of dynamical models. This is particularly the case for low-inclination galaxies like NGC 6958 (e.g. Lablanche et al. 2012; Bellovary et al. 2014). For those galaxies, the deprojection of the stellar surface brightness to the luminosity density is strongly degenerate (Rybicki 1987; Gerhard & Binney 1996) and the kinematics cannot properly constrain the anisotropy and mass (e.g. Lablanche et al. 2012). To evaluate possible systematics associated with the deprojection of the galaxy, we also constructed a Schwarzschild model assuming a nearly edge-on inclination (89°). The corresponding Schwarzschild models resulted in $M_{\rm BH} = (5.7^{+2.0}_{-1.0}) \times 10^8$ M$_\odot$ and M/L $= 0.87 \pm 0.03$ M$_\odot$/L$_\odot$, which was the highest black hole mass that we got from all of our tests with the Schwarzschild models. $M_{\rm BH} = 5.7 \times 10^8$ M$_\odot$ is still within the 3σ measurement uncertainties and NGC 6958 is clearly not an edge-on galaxy, such that we decided to not enhance the systematic uncertainties of the fiducial model due to this test.

4.4.3 *Systematics in the mass model*

Stellar mass model: As the mass model does not have associated errors, we tested how much using a different mass model changes the results. In Section 2.2, we described different imaging data that are available for NGC 6958. We constructed an alternative MGE model using the F814W image obtained with WFPC2 in combination with CGS (Ho et al. 2011; Li et al. 2011) imaging data. As bluer images are much more prone to dust extinction, using the F814W images required a detailed dust masking. We followed all steps described in Thater et al. (2017), applied a dust masking of attenuated pixels, fitted the surface brightness profile with MGE, and then created dynamical Schwarzschild and JAM models. We used the same set-up as in the fiducial model, inclination of 45°, increased kinematic errors for $R > 2$ arcsec, and stellar kinematics from the simultaneous fit of stellar absorption and gas emission. Evaluating these Schwarzschild models, we obtained a formal best fit of $M_{\rm BH} = (3.1^{+1.5}_{-1.3}) \times 10^8\,{\rm M}_\odot$ and $\rm M/L = 4.1 \pm 0.06\,M_\odot/L_{\odot,I}$, which is 15 per cent lower than using the mass model from near-infrared imaging, but consistent with the fiducial model results.

The results of this test agree with the conclusion from e.g. Nguyen et al. (2018, 2019) that taking different mass models into account does not significantly alter the mass measurements provided that both mass models are created from images that have a spatial resolution close to the black hole SoI (Yoon 2017) and a careful treatment of dust attenuation was applied (e.g. Cohn et al. 2021).

M_*/L gradients: In the dynamical models that we presented so far, we assumed a constant dynamical M/L within the MUSE FoV. However, observations have shown that most early-type galaxies have negative stellar M/L (M_*/L) gradients from the centre towards larger radii (e.g. Tortora et al. 2011; Li et al. 2018). With an effective radius of 15.″3 and a galaxy mass of $8 \times 10^{10}\,{\rm M}_\odot$, we expect a small negative gradient for NGC 6958 (fig. 7 of Li et al. 2018). On the other hand, the presence of nuclear molecular gas might lead to ongoing nuclear star formation (Crocker et al. 2011) that would indicate a lower M_*/L in the galaxy centre (Davis & McDermid 2017). An M_*/L gradient for NGC 6958 is therefore expected. If the change in the M_*/L profile is of the order of 10 per cent, the ignorance of M/L gradients in the dynamical models can lead to a significant underestimation of the stellar mass in the centre and thus an overestimation of the black hole mass. McConnell et al. (2013) and Thater et al. (2019) included radially varying M_*/L in their dynamical models and noted a decrease in $M_{\rm BH}$ by up to 30 per cent, while Cappellari et al. (2002) found negligible effects.

We followed the approach of Thater et al. (2019), derived M_*/L profiles for NGC 6958 from the full-spectrum fitting of the MUSE observations, and included the M_*/L variation in our dynamical models. We utilized the PPXF routine and fitted a linear combination of MILES Single Stellar Population (SSP) models (Version 11.0; Vazdekis et al. 2016) to the co-added MUSE spectra within circular apertures with radii between 0.″5 and 29.″5. We used two different SSP model libraries assuming Padova isochrones (Girardi et al. 2000) and (1) a Salpeter (1955) initial mass function (IMF) and (2) a Kroupa (2001)-revised IMF. For each of the two IMF choices, we used template spectra in a regular grid of log (age) between 0.1 and 14.1 Gyr and metallicities ([Z/H]) between −1.71 and 0.22 dex. Note that compared to our previous study (Thater et al. 2019), we cut the grid to the safe age ranges specified at the MILES website.[8] We then fitted those SSP templates to our MUSE spectra between

[8] http://research.iac.es/proyecto/miles//pages/ssp-models/safe-ranges.php

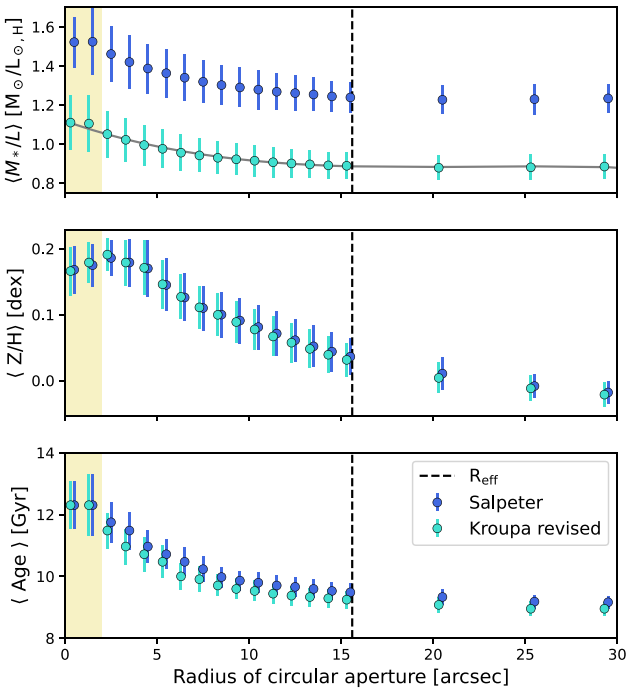

Figure 11. Stellar M/L in the *H* band, metallicity, and age profiles of NGC 6958 derived from stellar population analysis of the MUSE data. The two different colours specify whether the MILES SSP templates were calculated with a Salpeter IMF (blue) or a revised Kroupa IMF (cyan). The grey line through the Kroupa-revised IMF-based M_*/L values is the third-order polynomial fit derived in Section 4.4.3. The dashed line denotes the effective radius of NGC 6958, while the yellow shaded area shows where dust is affecting the results (<2 arcsec).

4820 and 6820 Å and masked the same regions as for the kinematics extraction (Section 3.2). Due to a template mismatch caused by bad fits in the red wavelength range, we added a 'red' mask to cover the region between 6350 and 6570 Å. This template mismatch remains when adding additional lines like [Fe X] to the PPXF fit. Our age determination is strongly driven by the H β absorption line at a rest-frame wavelength of 4861 Å that is contaminated by the H β gas emission line. To obtain a robust age estimate, we did not mask the emission lines but added the Balmer lines and forbidden emission lines to the fit. The Balmer lines were assumed to follow a characteristic theoretical Balmer decrement (case B recombination with $T = 10^4$ K, $n = 100$ cm^{-3}), but were allowed to vary their relative intensities following a Calzetti et al. (2000) reddening curve. As in Thater et al. (2019), we also made use of the regularization to the weights in age and metallicity to derive a smooth star formation history (SFH). The uncertainties were determined from the difference between regularized and non-regularized solutions.

Fig. 11 shows the mass-weighted M_*/L, age, and metallicity profiles extracted for the two different IMFs. Like Thater et al. (2019), we see a similar trend in the M_*/L gradients for the two IMFs but a difference of about $0.4\,{\rm M}_\odot/{\rm L}_\odot$, the M_*/L of the Kroupa-revised IMF being lower. The stellar M_*/L derived from the Salpeter IMF are not consistent with the dynamical M/L from our dynamical models and we will use the stellar M_*/L from the Kroupa-revised IMF for the rest of this section. A 'light' Milky-Way-like IMF like a Kroupa IMF appears to better describe the low- to intermediate-dispersion ellipticals (Cappellari et al. 2012, 2013; Lyubenova et al. 2016; Li, Sellwood & Shen 2017), which is confirmed for NGC 6958 by our

dynamical modelling results. We derived stellar M_*/L values from $1.12\,M_\odot/L_\odot$ in the centre to $0.88\,M_\odot/L_\odot$ at about 30 arcsec, which are consistent with the dynamical M/L from our dynamical models. Driven by variations in metallicity and age, we see a clear stellar M_*/L decrease of 20 per cent within the bulge effective radius, flattening out at larger radii. The shape of the M_*/L can be well parametrized by a third-order polynomial.[9] For $R < 2$ arcsec, our derived values were strongly affected by the nuclear dust disc of the galaxy, and we excluded those values in the fit. We then multiplied each component j of our MGE with the interpolated stellar M/L_* at the corresponding σ_j radius of the MGE component and included this mass density into the dynamical models. From these new models, we obtained a black hole mass of $(2.9^{+2.2}_{-1.8}) \times 10^8\,M_\odot$ in the Schwarzschild models, resulting in an about 20 per cent decrease in mass. A radially varying stellar M/L_* is usually not explicitly included in the dynamical models when deriving black hole masses. However, when the total mass profile is allowed to differ from the distribution of the tracer population (e.g. by including a dark matter profile), the change in M/L_* can be accounted for as well. Furthermore, the difference to the models with constant M/L is so small, that the models with radially varying M/L lie within the 3σ uncertainties of our reported measurements.

When inspecting the SFHs at different distances from the centre (Fig. 12), we noticed a second younger stellar component of about 4 Gyr that starts to be visible at 5 arcsec. The SFH might also reveal a third low-mass component at an age of about 1.5 Gyr, possibly the remnant of a recent minor merger that has also been discussed in the literature (Malin & Carter 1983; Saraiva et al. 1999). However, the 1.5 Gyr-old stellar component is very uncertain as it appears only in a single age and metallicity bin. As it is only visible at radii larger than 15 arcsec, this young component does not affect our dynamical models.

4.4.4 *Conclusion of the systematics and alignment of the velocity ellipsoid*

In the previous subsections, we analysed several sources of uncertainty. While some of them gave negligible deviations from the main result $M_{\rm BH} = (3.6^{+2.5}_{-1.3}) \times 10^8\,M_\odot$, for others we noticed significant differences that we included as additional systematic uncertainty in our final result. We found a confirmation of our main result by accounting for differences in the kinematics extraction (except for going into the blue region) and also by using different mass models. However, strong biases for both used dynamical modelling methods are evident from the mass deprojection at such a low inclination. Taking all tested systematics into account, we report $M_{\rm BH} = (3.6^{+2.7}_{-2.4}) \times 10^8\,M_\odot$ at 3σ significance as final result of the Schwarzschild models. This measurement is consistent with our $\rm JAM_{sph}$ models that resulted in more massive black holes of $M_{\rm BH} = (4.6^{+2.5}_{-2.7}) \times 10^8\,M_\odot$ and inconsistent with $M_{\rm BH} = (8.6^{+0.8}_{-0.8}) \times 10^8\,M_\odot$ from $\rm JAM_{cyl}$. One difference between the models is the alignment of the velocity ellipsoid. Compared to JAM, the velocity ellipsoid does not have a fixed alignment in the Schwarzschild models. The tilt angle α of the velocity ellipsoid can be derived from the components of the velocity tensor via $\tan 2\alpha = 2\langle v_r v_\theta \rangle / (\langle v_r^2 \rangle - \langle v_\theta^2 \rangle)$, where the components are an output from the Schwarzschild models (see e.g. Cappellari et al. 2007). α measures the deviation from spherical alignment, which corresponds to $\alpha = 0°$. An analogous tilt angle can also be defined for cylindrical coordinates (see e.g. Cappellari 2008; Smith, Evans & An 2009). Fig. 13 shows the misalignment of the Schwarzschild velocity ellipsoid from cylindrical and spherical alignment for our best-fitting model. We also explored the axial ratio of the velocity ellipsoid (Cappellari 2008) and found ranges between 0.65 and 0.9, which indicates that the misalignment is not negligible. It is clearly visible that the velocity ellipsoid has a varying orientation, which was also seen in axisymmetric Schwarzschild models for other galaxies (Cappellari et al. 2007). Furthermore, the velocity ellipsoid of our Schwarzschild model of NGC 6958 is more consistent with spherical alignment, which could explain why the spherical-aligned JAM models give an $M_{\rm BH}$ that is closer to the measurement from Schwarzschild.

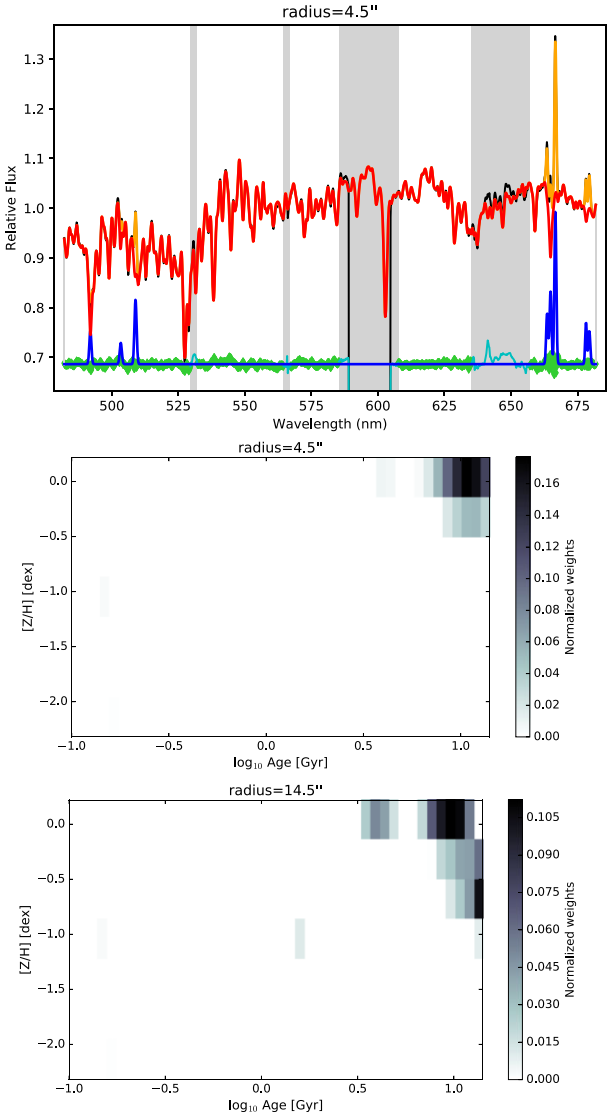

Figure 12. Results of the stellar population analysis. Top: A comparison between the integrated MUSE spectrum (black) and the spectral fit (red). The representation of the components is the same as Fig. 4. Bottom: Mass-weighted SFHs (age and metallicity bins that contribute to the spectral fitting). The greyscale shows the normalized weights of the models. Both panels were chosen to reflect the contribution at the edge of our kinematics.

[9] $(M_*/L\ /{\rm M}_\odot/{\rm L}_{\odot,{\rm H}}) = (1.12\text{–}3.29) \times 10^{-2} \times ({\rm arcsec}) + 1.50 \times 10^{-3} \times ({\rm arcsec})^2 - 2.24 \times 10^{-5} \times ({\rm arcsec})^3$ for $R \leq 30$ arcsec and constant $0.89\,M_\odot/L_\odot$ for $R > 30$ arcsec.

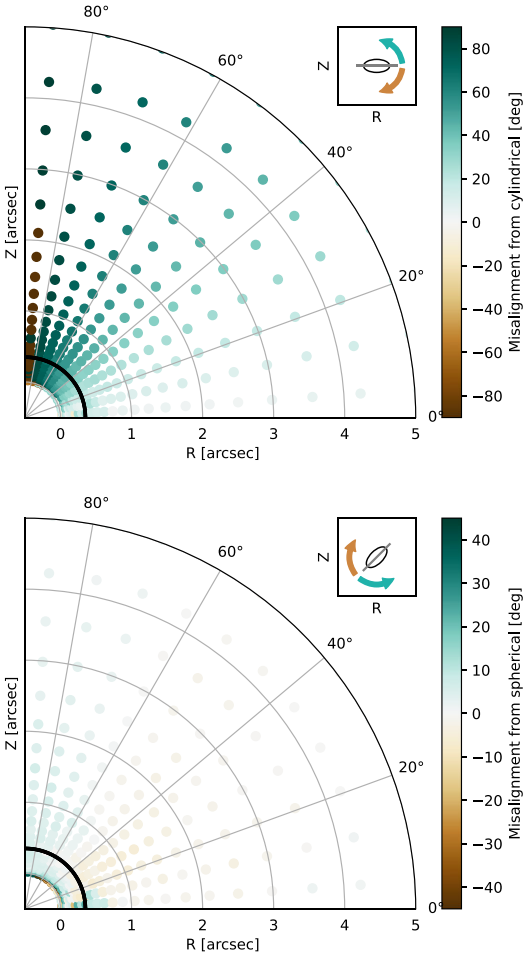

Figure 13. The alignment of the velocity ellipsoid from the best-fitting Schwarzschild model in the meridional plane projection. The upper panel shows the misalignment from a cylindrical-aligned velocity ellipsoid. We show the non-tilted version in the inset in the top right of the panel. Both arrows in the inset indicate the direction of the misalignment. The bottom panel shows the misalignment from a spherical-aligned velocity ellipsoid (example again in the inset). The values within the black curve are affected by the PSF.

4.4.5 The influence of dark matter

Our dynamical models assume self-consistence (mass follows light). Breaking this assumption by including dark matter as additional component in the dynamical models can lead to systematic changes in the black hole mass if $R_{\rm SoI}$ is not well resolved (Gebhardt & Thomas 2009; Gebhardt et al. 2011; Schulze & Wisotzki 2011; Rusli et al. 2013). NGC 6958 lies in a similar mass range as the galaxies that we analysed in Thater et al. (2019), in particular NGC 584 and NGC 2784. It is therefore expected that dark matter has only a negligible contribution within the FoV of our kinematic tracer. Analogous to our previous study, we used the radial acceleration relation (McGaugh, Lelli & Schombert 2016; Lelli et al. 2017) and calculated the total acceleration from our MGE model yielding $g_{\rm dyn} = 1.3 \times 10^{-9}\,{\rm m\,s^{-2}}$. As long as a galaxy stays in the linear regime of the radial acceleration relation ($g_{\rm dyn} > g_{\rm crit} = 1.2 \times 10^{-10}\,{\rm m\,s^{-2}}$), it is expected that dark matter only marginally affects the dynamics. Based on the calculated $g_{\rm dyn}$, NGC 6958 lies within the linear regime of the radial acceleration relation. However, the dark matter halo will influence orbits that not only go beyond the probed radii, but also come close to the SMBH. This might explain the tendency for moderately larger $M_{\rm BH}$ in the $\rm JAM_{sph}$ models compared to Schwarzschild models that cover almost one effective radius of NGC 6958.

We decided to test this hypothesis by running the fiducial Schwarzschild models with a Navarro–Frank–White (NFW; Navarro, Frenk & White 1996) dark halo. We used a similar approach to the one described in Cappellari et al. (2013), which in their study was applied to JAM models. We assumed that the dark matter follows a two-parameter power-law NFW profile with a spherical shape. The NFW can then be parametrized as a function of the halo mass (M_{200}) and the halo concentration (c_{200}) that are connected via the M_{200}–c_{200} relation (Navarro et al. 1996). We used equation (8) by Dutton & Macciò (2014) in order to make the halo profile a function of only one free parameter, M_{200}. We then fitted a one-dimensional MGE to this profile and added those MGE parameters to the galaxy potential in the Schwarzschild models. The Schwarzschild models were run in a three-dimensional grid ($M_{\rm BH}$, $\rm M_*/L$, M_{200}). Note that in this run $\rm M_*/L$ is the stellar M/L and not the dynamical M/L anymore. For $M_{\rm BH}$ and $\rm M_*/L$, we kept the grid values from Section 4.2, while the M_{200} grid values were varied between 10^{12} and 10^{14} $\rm M_\odot$, which is expected for a galaxy of $\approx 10^{11}$ $\rm M_\odot$ stellar mass based on abundance matching (Moster, Naab & White 2013). In order to test the effects of very massive (and physically unrealistic) haloes, we extended the M_{200} grid to 10^{16} $\rm M_\odot$. Compared to the main runs in this paper, for this test we sampled the orbits in a smaller orbit library with 21 logarithmically spaced orbit energies, 8 linearly spaced orbit angular momenta L_z, and 7 linearly spaced non-classical third integral values I3. The smaller orbit library does not change the best-fitting values but mostly has an effect on the contour shape of the χ^2 distribution, and is therefore sufficient for this test.

The resulting Schwarzschild grids are shown in Fig. D1. The degeneracy between $M_{\rm BH}$, $\rm M_*/L$, and M_{200} is clearly visible. With increasing dark matter fraction, the $\rm M_*/L$ decreases and $M_{\rm BH}$ increases. However, it is not possible with our MUSE data set (covering one effective radius of NGC 6958) to put constraints on the dark matter, and the best-fitting χ^2 values of the different grids are very similar. Small fluctuations between the χ^2 values are likely caused by numerical errors. The trends of these models and a comparison with the JAM result are shown in Fig. 14. Within a dark matter fraction that is consistent with abundance matching, the change in black hole mass is not significant and stays within the uncertainties that were given in the previous tests. Furthermore, taking into account dark matter in Schwarzschild models would remove the remaining small difference between Schwarzschild and $\rm JAM_{sph}$ models. The discrepancy with $\rm JAM_{cyl}$ cannot be explained with dark matter as it would require unrealistically high dark matter mass haloes (matching those of massive galaxy clusters), and seems to predominantly follow from the assumption of the velocity ellipsoid as discussed in Section 4.4.4.

Fig. 14 also shows the effect of the inclusion of dark matter on the measured $\rm M_*/L$. Contrary to Fig. 8, the M/L from JAM is now larger or equal to that from Schwarzschild. This is because the M/L from JAM is a total value, while that from Schwarzschild's models is the $\rm M_*/L$ of the stars alone. Fig. D1 shows that when the dark halo is small and the stars dominate the total mass in the Schwarzschild models, the M/L from JAM and Schwarzschild's models agree well. However, when the dark matter contribution increases, the stellar $\rm M_*/L$ must correspondingly decrease as observed. Specifically, the stellar and total M/L are approximately related as (equation 23 of Cappellari et al. 2013)

$$(\rm M/L)_{JAM} \approx (M_*/L)/[1 - f_{DM}(r = R_{JAM})], \quad (1)$$

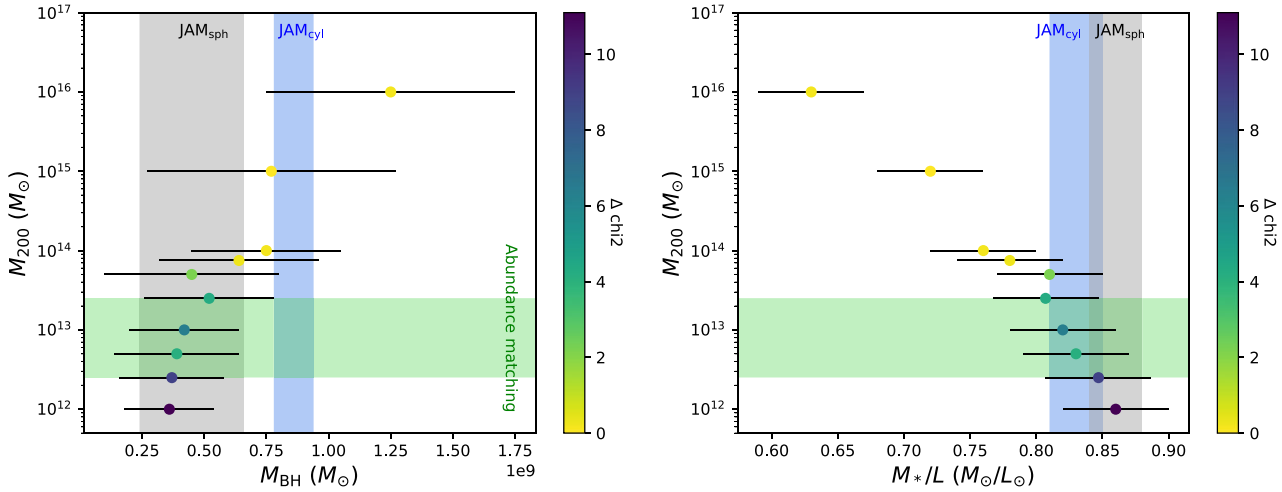

Figure 14. The effect of dark matter on the measured black hole mass and M/L in the Schwarzschild models. Every point is the best-fitting Schwarzschild measurement of one of the grids shown in Appendix E. The colour specifies the $\Delta\chi^2$ between the best-fitting model and the minimum χ^2 of all Schwarzschild models + dark matter. All Schwarzschild results are compared with the best-fitting results from JAM with spherically (grey) and cylindrically (blue) aligned velocity ellipsoid. Note that with JAM, we measured a dynamical M/L.

where $f_{DM}(r = R_{JAM})$ is the fraction of dark matter enclosed within the region fitted by the JAM models.

From the χ^2 distribution of our Schwarzschild models, it is not possible to solve the M_{BH}–M_{200} degeneracy. That is why we tried to quantify the effect of dark matter on the black hole mass by creating a Gaussian prior from the abundance matched dark halo values and multiplying this prior probability with the likelihood probability of the dynamical models (similar to a Bayesian analysis):

$$P_{\rm posterior}(\text{Model} \mid M_{\rm BH}, M_*/L, M_{200}) \propto P_{\rm likelihood} \cdot P_{\rm prior}(M_{200}). \quad (2)$$

NGC 6958 has a galaxy mass of $(8.6 \pm 2.0) \times 10^{10}$ $M_\odot$ that results in $\log(M_{200}/M_\odot) = 12.9 \pm 0.4$. Together with a scatter in the abundance matching relation of 0.1 dex at $z = 0$ (Moster et al. 2013), we obtained a Gaussian prior with $\mu = \log(M_{200}/M_\odot) = 12.9$ and $\sigma = 0.5$. The likelihood can be directly inferred from the χ^2 distribution of the dynamical models. The posterior probability is then calculated as

$$\ln P_{\rm posterior} \propto -\chi^2/2 + \ln P_{\rm prior}. \quad (3)$$

We then assumed that we can compute confidence levels on $P_{\rm posterior}$ as usually done on the likelihood alone. Adopting the minimum of $\ln P_{\rm posterior}$ as our best-fitting value, we obtained $M_{\rm BH,DM} = (4.5 \pm 2) \times 10^8$ $M_\odot$. This value is 25 per cent larger than $M_{\rm BH}$ from the fiducial Schwarzschild models but fully consistent with those results. This test confirms that the inclusion of dark matter in our dynamical models does not significantly change our final results.

5 DISCUSSION AND CONCLUSION

5.1 Black hole scaling relations

Together with the derived effective velocity dispersion, our estimated black hole mass $(3.6^{+2.7}_{-2.4}) \times 10^8$ $M_\odot$ from the Schwarzschild models can be compared with dynamical black hole masses from the literature (most recent compilation by Sahu, Graham & Davis 2019). We first compared our $M_{\rm BH}$ measurement with predictions from the bulge effective velocity dispersion of 168 km s^{-1} with different scaling relations. Using the scaling relation by Saglia et al. (2016) for power-law early-type galaxies, we estimated $(1.1 \pm 0.2) \times 10^8$ $M_\odot$, where the uncertainty was derived from the uncertainty in the velocity dispersion. A similar black hole mass was estimated for the scaling relation in van den Bosch (2016). However, our mass measurement turned out to be three times more massive. On the other hand, Sahu et al. (2019) used the central velocity dispersion in their black hole scaling relation analysis to correct for possible contamination of disc rotation. We also derived the central velocity dispersion of NGC 6958 (within 1.95 arcsec) yielding 220 ± 5 km s^{-1}. Inserting this value into their black hole mass–central velocity dispersion relation for early-type galaxies gives $(3.6 \pm 0.5) \times 10^8$ $M_\odot$. Our derived black hole mass is therefore neither strongly overmassive nor undermassive when compared to the bulk of literature black hole masses given NGC 6958's central velocity dispersion. We also compared our mass measurement with the black hole mass–bulge mass relation from Saglia et al. (2016) for power-law early-type galaxies. Given NGC 6958's bulge mass of $(3.6 \pm 1.4) \times 10^{10}$ $M_\odot$ (Table 1), this relation yields a black hole mass of $(1.1 \pm 0.9) \times 10^8$ $M_\odot$. Again, our measurement is overmassive compared to the scaling relations but we might underestimate the bulge mass due to the limited FoV. Furthermore, our measurement is consistent with the general scatter of black hole masses at $\sigma_{\rm e,star} \approx 200$ km s^{-1}. We will further discuss the implications of our measurement in the context of the scaling relations and galaxy assembly in Thater et al. (in preparation), where we will use gas kinematics as an independent tracer to derive the black hole mass.

5.2 Summary of our results

We have presented our central black hole mass measurement of the lenticular galaxy NGC 6958. For that purpose, we obtained AO-assisted MUSE science verification data and extracted ionized gas and stellar kinematics maps. We used Gaussian LOSVDs for the ionized gas kinematics and LOSVDs parametrized as Gauss–Hermite polynomials up to the order of 6 for the stellar kinematics extraction. The ionized gas kinematics have a clear velocity dispersion peak of 270 km s^{-1} and a regular rotational velocity within 5 arcsec. However, at greater distance from the centre, we notice strongly disturbed

features in the gas rotational velocity map, dominated by receding motion. On the other hand, our stellar kinematic maps show very regular rotation within 15 arcsec with a maximal rotational velocity of 130 km s^{-1} and a clear and distinct velocity dispersion peak of 250 km s^{-1}. We combined the extracted stellar kinematics with high-resolution NICMOS F160W images and created axisymmetric Jeans anisotropic and Schwarzschild models. Jeans anisotropic models gave best-fitting black hole masses of $(4.6^{+2.5}_{-2.7}) \times 10^8$ and $(8.6^{+0.8}_{-0.8}) \times 10^8\,M_\odot$ for spherical and cylindrical alignments of the velocity ellipsoid, respectively. From our Schwarzschild models, we estimated a black hole mass of $(3.6^{+2.7}_{-2.4}) \times 10^8\,M_\odot$ and a constant dynamical M/L of $0.91 \pm 0.04\,M_\odot/L_{\odot,H}$. Two of our three determinations are consistent within their uncertainties, while only JAM_{cyl} is slightly inconsistent. When using a radially varying M/L in our dynamical models, we obtained a black hole mass 20 per cent lower than the fiducial models. When adding a dark halo (based on abundance matching) to our Schwarzschild models, the black hole mass increases by 25 per cent. Our derived black hole mass is overmassive compared to most scaling relation but agrees with the M_{BH}–$\sigma_{e,star}$ relation within 3σ. We carefully discuss the systematics with the kinematic data, the mass model, and the dynamical models in Section 4 and conclude that we fully cover the discussed systematics in our associated uncertainties. The most dominant effects were found to come from inconsistencies in the stellar kinematics extraction (when using only the 'blue' spectral range), the well-known problem of the inclination–mass deprojection degeneracy in low-inclination galaxies and model-dependent differences. In a companion paper, we will derive the SMBH mass in NGC 6958 using ionized and molecular gas as dynamical tracers. A cross-check of the three measurements will help to constrain the black hole mass and provide additional value in understanding whether the scatter in the black hole scaling relations is strongly affected by measurements from different measurement methods.

ACKNOWLEDGEMENTS

We thank the anonymous referee for the detailed referee report that improved the quality of this manuscript. We thank Tadeja Veršič for illuminating discussions on dark matter in dynamical models. ST acknowledges funding from the TAIZAI Visiting Fellowship during the Spring 2018 at National Observatory of Japan and the Deutsche Forschungsgemeinschaft (DFG) Grant KR 4548/1-1. Furthermore, part of this research was supported by the European Union's Horizon 2020 research and innovation programme under grant agreement number 724857 (Consolidator Grand ArcheoDyn). PMW was supported by Bundesministerium für Bildung, Wissenschaft und Forschung (BMBF) Verbundforschung (MUSE-NFM Project, grant 05A17BAA). MB was supported by Science and Technology Facilities Council (STFC) consolidated grant 'Astrophysics at Oxford' ST/H002456/1 and ST/K00106X/1. TAD acknowledges support from the UK Science and Technology Facilities Council through grant ST/S00033S/1. This work is based on observations collected at the European Organisation for Astronomical Research in the Southern hemisphere under ESO programme 60.A-9193(A) and also based on observations made with the NASA/ESA *HST*, obtained from the Hubble Legacy Archive, which is a collaboration between the Space Telescope Science Institute (STScI/NASA), the Space Telescope European Coordinating Facility (STECF/ESA), and the Canadian Astronomy Data Centre (CADC/NRC/CSA). This research has made use of the NASA/IPAC Extragalactic Database (NED) that is operated by the Jet Propulsion Laboratory, California Institute of Technology, under contract with the National Aeronautics and Space Administration. This research is partially based on data from the MILES project.

DATA AVAILABILITY

Raw MUSE data are available in the ESO archive. Kinematics are available from the author on reasonable request.

REFERENCES

Ahn C. P. et al., 2018, ApJ, 858, 102
Annibali F., Bressan A., Rampazzo R., Zeilinger W. W., Vega O., Panuzzo P., 2010, A&A, 519, A40
Bacon R. et al., 2010, in McLean I. S., Ramsay S. K., Takami H., eds, Proc. SPIE Conf. Ser. Vol. 7735, Ground-Based and Airborne Instrumentation for Astronomy III. SPIE, Bellingham, p. 773508
Bacon R. et al., 2017, A&A, 608, A1
Barth A. J., Darling J., Baker A. J., Boizelle B. D., Buote D. A., Ho L. C., Walsh J. L., 2016, ApJ, 823, 51
Beifiori A., Courteau S., Corsini E. M., Zhu Y., 2012, MNRAS, 419, 2497
Bellovary J. M., Holley-Bockelmann K., Gültekin K., Christensen C. R., Governato F., Brooks A. M., Loebman S., Munshi F., 2014, MNRAS, 445, 2667
Boizelle B. D., Barth A. J., Walsh J. L., Buote D. A., Baker A. J., Darling J., Ho L. C., 2019, ApJ, 881, 10
Boizelle B. D. et al., 2021, ApJ, 908, 19
Calzetti D., Armus L., Bohlin R. C., Kinney A. L., Koornneef J., Storchi-Bergmann T., 2000, ApJ, 533, 682
Cappellari M., 2002, MNRAS, 333, 400
Cappellari M., 2008, MNRAS, 390, 71
Cappellari M., 2017, MNRAS, 466, 798
Cappellari M., 2020, MNRAS, 494, 4819
Cappellari M., Copin Y., 2003, MNRAS, 342, 345
Cappellari M., Emsellem E., 2004, PASP, 116, 138
Cappellari M., Verolme E. K., van der Marel R. P., Verdoes Kleijn G. A., Illingworth G. D., Franx M., Carollo C. M., de Zeeuw P. T., 2002, ApJ, 578, 787
Cappellari M. et al., 2006, MNRAS, 366, 1126
Cappellari M. et al., 2007, MNRAS, 379, 418
Cappellari M. et al., 2009, ApJ, 704, L34
Cappellari M. et al., 2012, Nature, 484, 485
Cappellari M. et al., 2013, MNRAS, 432, 1709
Cohn J. H. et al., 2021, ApJ, 919, 77
Crocker A. F., Bureau M., Young L. M., Combes F., 2011, MNRAS, 410, 1197
Davies R. I., Müller Sánchez F., Genzel R., Tacconi L. J., Hicks E. K. S., Friedrich S., Sternberg A., 2007, ApJ, 671, 1388
Davis T. A., McDermid R. M., 2017, MNRAS, 464, 453
Davis T. A., Bureau M., Cappellari M., Sarzi M., Blitz L., 2013, Nature, 494, 328
Davis T. A., Bureau M., Onishi K., Cappellari M., Iguchi S., Sarzi M., 2017, MNRAS, 468, 4675
Davis T. A. et al., 2018, MNRAS, 473, 3818
Davis T. A. et al., 2020, MNRAS, 496, 4061
de Francesco G., Capetti A., Marconi A., 2006, A&A, 460, 439
den Brok M., Krajnović D., Emsellem E., Brinchmann J., Maseda M., 2021, MNRAS, 508, 4786
de Vaucouleurs G., de Vaucouleurs A., Corwin H. G. Jr, Buta R. J., Paturel G., Fouqué P., 1991, Third Reference Catalogue of Bright Galaxies. Volume I: Explanations and References. Volume II: Data for Galaxies between 0^h and 12^h. Volume III: Data for Galaxies between 12^h and 24^h. Springer, New York, USA
Drehmer D. A., Storchi-Bergmann T., Ferrari F., Cappellari M., Riffel R. A., 2015, MNRAS, 450, 128
Dutton A. A., Macciò A. V., 2014, MNRAS, 441, 3359

Falcón-Barroso J., Sánchez-Blázquez P., Vazdekis A., Ricciardelli E., Cardiel N., Cenarro A. J., Gorgas J., Peletier R. F., 2011, A&A, 532, A95
Feldmeier A. et al., 2014, A&A, 570, A2
Feldmeier-Krause A., Zhu L., Neumayer N., van de Ven G., de Zeeuw P. T., Schödel R., 2017, MNRAS, 466, 4040
Ferrarese L., Ford H. C., Jaffe W., 1996, ApJ, 470, 444
Foreman-Mackey D., Hogg D. W., Lang D., Goodman J., 2013, PASP, 125, 306
Fusco T. et al., 2020, A&A, 635, A208
Gao H., Ho L. C., 2017, ApJ, 845, 114
Gebhardt K., Thomas J., 2009, ApJ, 700, 1690
Gebhardt K., Adams J., Richstone D., Lauer T. R., Faber S. M., Gültekin K., Murphy J., Tremaine S., 2011, ApJ, 729, 119
Gerhard O. E., Binney J. J., 1996, MNRAS, 279, 993
Ghez A. M. et al., 2008, ApJ, 689, 1044
Gillessen S., Eisenhauer F., Trippe S., Alexander T., Genzel R., Martins F., Ott T., 2009, ApJ, 692, 1075
Gillessen S. et al., 2017, ApJ, 837, 30
Girardi L., Bressan A., Bertelli G., Chiosi C., 2000, A&AS, 141, 371
Greene J. E. et al., 2016, ApJ, 826, L32
Guérou A. et al., 2017, A&A, 608, A5
Ho L. C., Li Z.-Y., Barth A. J., Seigar M. S., Peng C. Y., 2011, ApJS, 197, 21
Holtzman J. A., Burrows C. J., Casertano S., Hester J. J., Trauger J. T., Watson A. M., Worthey G., 1995, PASP, 107, 1065
Huang S., Ho L. C., Peng C. Y., Li Z.-Y., Barth A. J., 2013, ApJ, 766, 47
Husser T. O., Wende-von Berg S., Dreizler S., Homeier D., Reiners A., Barman T., Hauschildt P. H., 2013, A&A, 553, A6
Knapen J. H., Comerón S., Seidel M. K., 2019, A&A, 621, L5
Kormendy J., Ho L. C., 2013, ARA&A, 51, 511
Krajnović D., Cappellari M., Emsellem E., McDermid R. M., de Zeeuw P. T., 2005, MNRAS, 357, 1113
Krajnović D., Cappellari M., de Zeeuw P. T., Copin Y., 2006, MNRAS, 366, 787
Krajnović D., McDermid R. M., Cappellari M., Davies R. L., 2009, MNRAS, 399, 1839
Krajnović D. et al., 2018, MNRAS, 477, 3030
Krist J., Hook R., 2001, The Tiny Tim User's Manual, Version 6.3
Kroupa P., 2001, MNRAS, 322, 231
Kuo C. Y. et al., 2011, ApJ, 727, 20
Lablanche P.-Y. et al., 2012, MNRAS, 424, 1495
Laurikainen E., Salo H., Buta R., Knapen J. H., Comerón S., 2010, MNRAS, 405, 1089
Lelli F., McGaugh S. S., Schombert J. M., Pawlowski M. S., 2017, ApJ, 836, 152
Li Z.-Y., Ho L. C., Barth A. J., Peng C. Y., 2011, ApJS, 197, 22
Li Z., Sellwood J. A., Shen J., 2017, ApJ, 850, 67
Li H. et al., 2018, MNRAS, 476, 1765
Lipka M., Thomas J., 2021, MNRAS, 504, 4599
Lyubenova M. et al., 2016, MNRAS, 463, 3220
McConnell N. J., Chen S.-F. S., Ma C.-P., Greene J. E., Lauer T. R., Gebhardt K., 2013, ApJ, 768, L21
McDermid R. M. et al., 2006, MNRAS, 373, 906
McGaugh S. S., Lelli F., Schombert J. M., 2016, Phys. Rev. Lett., 117, 201101
Madore B. F., Freedman W. L., Bothun G. D., 2004, ApJ, 607, 810
Malin D. F., Carter D., 1983, ApJ, 274, 534
Mehrgan K., Thomas J., Saglia R., Mazzalay X., Erwin P., Bender R., Kluge M., Fabricius M., 2019, ApJ, 887, 195
Mitzkus M., Cappellari M., Walcher C. J., 2017, MNRAS, 464, 4789
Miyoshi M., Moran J., Herrnstein J., Greenhill L., Nakai N., Diamond P., Inoue M., 1995, Nature, 373, 127
Moffat A. F. J., 1969, A&A, 3, 455
Moster B. P., Naab T., White S. D. M., 2013, MNRAS, 428, 3121
Navarro J. F., Frenk C. S., White S. D. M., 1996, ApJ, 462, 563
Neumayer N., Cappellari M., Reunanen J., Rix H., van der Werf P. P., de Zeeuw P. T., Davies R. I., 2007, ApJ, 671, 1329
Nguyen D. D. et al., 2017, ApJ, 836, 237
Nguyen D. D. et al., 2018, ApJ, 858, 118
Nguyen D. D. et al., 2019, ApJ, 872, 104
Nguyen D. D. et al., 2020, ApJ, 892, 68
Nguyen D. D. et al., 2021a, MNRAS, 509, 2920
Nguyen D. D. et al., 2021b, MNRAS, 504, 4123
Onishi K., Iguchi S., Sheth K., Kohno K., 2015, ApJ, 806, 39
Onishi K., Iguchi S., Davis T. A., Bureau M., Cappellari M., Sarzi M., Blitz L., 2017, MNRAS, 468, 4663
Onken C. A. et al., 2014, ApJ, 791, 37
Pastorini G. et al., 2007, A&A, 469, 405
Rusli S. P. et al., 2013, AJ, 146, 45
Rybicki G. B., 1987, in de Zeeuw P. T., ed., Proc. IAU Symp. 127, Structure and Dynamics of Elliptical Galaxies. Kluwer, Dordrecht, p. 397
Saglia R. P. et al., 2016, ApJ, 818, 47
Sahu N., Graham A. W., Davis B. L., 2019, ApJ, 887, 10
Salpeter E. E., 1955, ApJ, 121, 161
Sánchez-Blázquez P. et al., 2006, MNRAS, 371, 703
Sandage A., Bedke J., 1994, The Carnegie Atlas of Galaxies, Vol. I and II. Carnegie Institution of Washington
Saraiva M. F., Ferrari F., Pastoriza M. G., 1999, A&A, 350, 399
Saraiva M. F., Bica E., Pastoriza M. G., Bonatto C., 2001, A&A, 376, 43
Sarzi M. et al., 2006, MNRAS, 366, 1151
Schlafly E. F., Finkbeiner D. P., 2011, ApJ, 737, 103
Schulze A., Wisotzki L., 2011, A&A, 535, A87
Schwarzschild M., 1979, ApJ, 232, 236
Shapiro K. L., Cappellari M., de Zeeuw T., McDermid R. M., Gebhardt K., van den Bosch R. C. E., Statler T. S., 2006, MNRAS, 370, 559
Smith M. C., Evans N. W., An J., 2009, ApJ, 698, 1110
Ströbele S. et al., 2012, in Ellerbroek B. L., Marchetti E., Véran J.-P., eds, Proc. SPIE Conf. Ser. Vol. 8447, Adaptive Optics Systems III. SPIE, Bellingham, p. 844737
Tal T., van Dokkum P. G., Nelan J., Bezanson R., 2009, AJ, 138, 1417
Thater S. et al., 2017, A&A, 597, A18
Thater S., Krajnović D., Cappellari M., Davis T. A., de Zeeuw P. T., McDermid R. M., Sarzi M., 2019, A&A, 625, A62
Thater S., Krajnović D., Nguyen D. D., Iguchi S., Weilbacher P. M., 2020, in Valluri M., Sellwood J. A., eds, Proc. IAU Symp. 353, Galactic Dynamics in the Era of Large Surveys. Kluwer, Dordrecht, p. 199
Thatte D., 2009, NICMOS Data Handbook v. 8.0
Tortora C., Napolitano N. R., Romanowsky A. J., Jetzer P., Cardone V. F., Capaccioli M., 2011, MNRAS, 418, 1557
van den Bosch R. C. E., 2016, ApJ, 831, 134
van den Bosch R. C. E., de Zeeuw P. T., 2010, MNRAS, 401, 1770
van den Bosch R. C. E., van de Ven G., 2009, MNRAS, 398, 1117
van der Marel R. P., Cretton N., de Zeeuw P. T., Rix H.-W., 1998, ApJ, 493, 613
Vazdekis A., Koleva M., Ricciardelli E., Röck B., Falcón-Barroso J., 2016, MNRAS, 463, 3409
Verdoes Kleijn G. A., van der Marel R. P., de Zeeuw P. T., Noel-Storr J., Baum S. A., 2002, AJ, 124, 2524
Walsh J. L., van den Bosch R. C. E., Barth A. J., Sarzi M., 2012, ApJ, 753, 79
Walsh J. L., Barth A. J., Ho L. C., Sarzi M., 2013, ApJ, 770, 86
Weilbacher P. M. et al., 2020, A&A, 641, A28
Willmer C. N. A., 2018, ApJS, 236, 47
Yoon I., 2017, MNRAS, 466, 1987

SUPPORTING INFORMATION

Supplementary data are available at *MNRAS* online.

Figure S1. Count profiles of the photometric data along the major axis overplotted with the best-fitting MGE models. The left MGE

is described in the main text, while the right MGE is described in Appendix A. Top: Count profiles of the photometric data along the major axis. Overplotted is the best-fitting MGE model (red line) and each Gaussian component (grey lines). The MGE model was built from the combined photometric information of NICMOS ($R \leq 7$ arcsec) and wide-field WFC3 ($R > 7$ arcsec) data. The vertical dashed line marks the 7 arcsec boundary. Bottom: Residuals of the MGE model: (Data-Model)/Data.

Figure S2. Comparison between symmetrized MUSE kinematics and best-fitting Schwarzschild model for $M_{\rm BH} = 3.6 \times 10^8$ $M_\odot$ and M/L = 0.91 $M_\odot/L_{\odot,H}$ of the fiducial run. From left to right: Mean velocity, velocity dispersion, h_3, h_4, h_5, and h_6 Gauss–Hermite moments. From top to bottom: Symmetrized data, best-fitting Schwarzschild model and residual maps. Residuals are defined as difference between the Schwarzschild model and observed kinematics divided by the observational errors. North is up and east to the left.

Figure S3. Same as Fig. S2, but zoom-in to the centre.

Figure S4. Results of the JAM modelling with cylindrical (left) and spherical (right) velocity ellipsoid alignment ordered into 2 × 2 panels. The top left panel shows the observed $V_{\rm rms}$ of NGC 6958, while the top right panel shows the best-fitting JAM model obtained from MCMC (fiducial model). Model and data are mostly in good agreement with each other, but the central $V_{\rm rms}$ is slightly too high. We also show models for a formally too low (bottom left) and too high $M_{\rm BH}$ (bottom right). Note that for $\rm JAM_{cyl}$, the lower mass black hole recovers the central $V_{\rm rms}$ quite well. Furthermore, both $\rm M_{cyl}$ and $\rm M_{sph}$ models can recover the observed $V_{\rm rms}$ equally well.

Figure S5. Comparison of the kinematic maps for the different kinematics extractions discussed in Section 4.4.1. From left to right, the panels show the S/rN, the rotational velocity after subtracting the systemic velocity, velocity dispersion, and $V_{\rm rms}$. From top to bottom, we show the kinematics extractions masking the gas emission lines, simultaneously fitting gas and stellar kinematics, 'blue' spectral region, and CaT spectral region. The second row is the extraction that we used for the main result of this paper. However, it is clear that the different approaches did not change the extracted kinematics significantly (except for 'blue'). North is up and east to the left.

APPENDIX A: MGE OF THE F814W WFPC2 + *i*-BAND CGS IMAGES

We followed a similar approach as in Section 4.1 to obtain a light model for NGC 6958 in the *i* band. As the *i* band is more affected by dust extinction than the *H* band, this light model required a careful treatment of the dust-affected galaxy centre. We therefore created a dust mask following the procedure given in Thater et al. (2017, 2019). We generated the surface brightness profile and iteratively fitted the lower envelope of the not-dust-affected regions with a four-parameter logistic function (see Fig. A1). Masked were all pixels that had a surface brightness below this envelope fit. We then applied the MGE routine (Cappellari 2002) simultaneously on the dust-masked WFPC2 and the CGS image as described in Section 4.1. In the central 10 arcsec, the MGE was constrained by the WFPC2 image, while the CGS image constrains the photometry at larger radii (Fig. S1 of the supplementary material). The WFPC2 image was used for the photometric calibration. For the conversion, we used 4.53 mag for the absolute AB magnitude of the sun (Willmer 2018) in the F814W band and $A_{\rm F814} = 0.07$ mag for the Galactic extinction (NED). TableA1 shows the derived MGE parameters. This MGE model was used in Section 3.1 to derive the PSF of the MUSE data and in Section 4.4.3 where we tested the effect of different mass models on the robustness of our black hole mass measurement.

Table A1. *HST*/WFPC2 F814W + *i*-band CGS MGE model.

j	$\log(I_j)$ ($L_{\odot,H}$ pc^{-2})	σ_j (arcsec)	q_j	$\log(M_j^{\rm const})$ ($M_\odot$)
(1)	(2)	(3)	(4)	(5)
1	5.136	0.041	0.91	8.186
2	4.699	0.146	0.90	8.853
3	4.169	0.416	0.91	9.239
4	3.912	0.924	0.89	9.664
5	3.609	1.807	0.87	9.934
6	2.833	3.806	0.86	9.803
7	2.654	7.209	0.86	10.179
8	2.056	15.081	0.88	10.227
9	1.39	31.787	0.91	10.226
10	− 1.263	83.174	0.91	8.408

Notes. Column 1: Index of the Gaussian component. Column 2: Surface brightness. Column 3: Projected Gaussian width along the major axis. Column 4: Projected axial ratio for each Gaussian component. Columns 5 and 6: Total mass of Gaussian component. In column (5), the constant dynamical M/L = 4.1 $M_\odot/L_\odot$ from the Schwarzschild modelling (Section 4.4.3) was used to determine the mass of each Gaussian component.

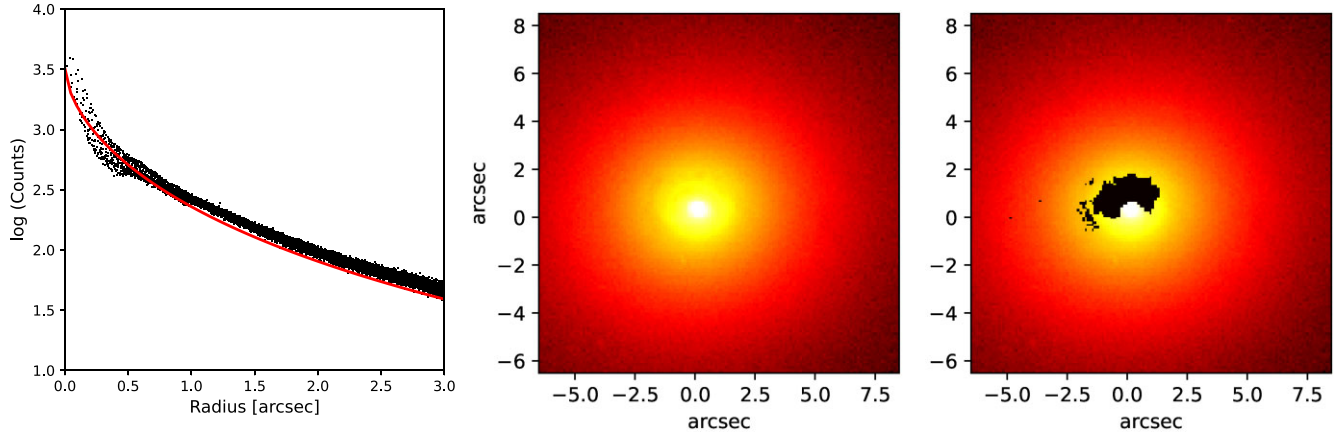

Figure A1. Dust masking of the F814W WFPC2 image. Left-hand panel: Every point is a pixel of the WFPC2 image, and the lower envelope fit of the surface brightness is given by the red solid line. Each pixel below the red line is masked when creating the MGE. Middle and right-hand panel: Central part of the *HST*/F814W image with and without dust mask.

APPENDIX B: DOUBLE GAUSSIAN PARAMETRIZATIONS OF THE MUSE PSF STAR

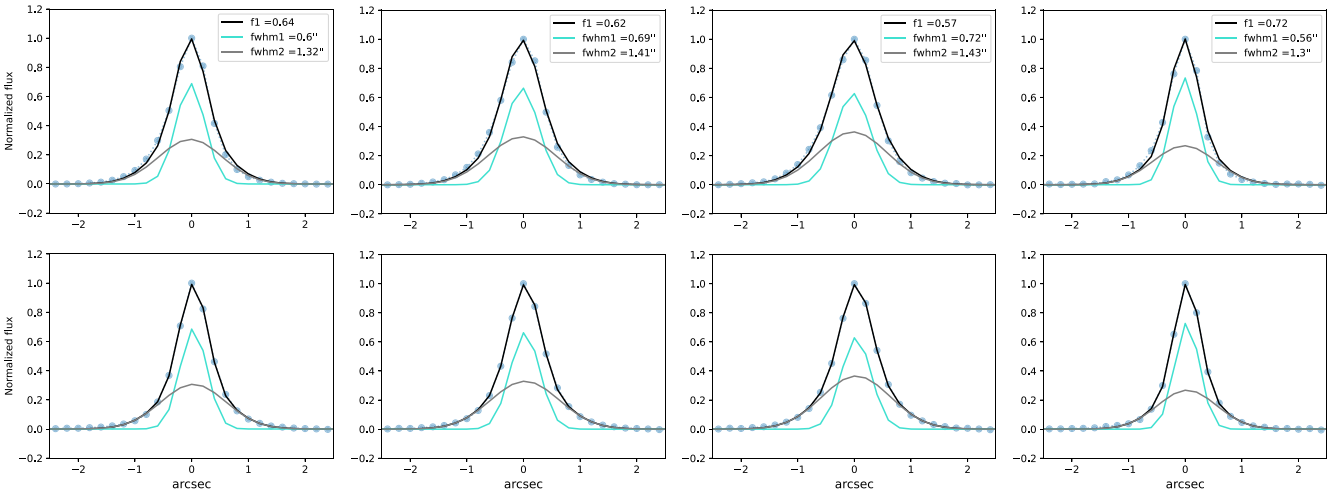

Figure B1. PSF parametrization of the PSF star close to NGC 6958 using a double Gaussian function. From left to right: White-light, optical, blue, and CaT wavelength image. Top is the cut along the major axis and bottom along the minor axis. The blue circles show the data points of the PSF star. The fits in different colours show the double Gaussian (black), the narrow Gaussian component (cyan), and the broad (grey) Gaussian component of the PSF. The Gaussians are characterized by their FWHM and the relative flux of the narrow Gaussian (f1).

APPENDIX C: JAM RESULT VALIDATION

Table C1. Results of the JAM measurement testing different systematics.

Velocity ellipsoid	Spectral range	i	Additional change	$M_{\rm BH}$ ($\times 10^8$ M$_\odot$)	M/L (M$_\odot$/L$_{\odot,\rm H}$)	β	χ^2/d.o.f.
(1)	(2)	(3)	(4)	(5)	(6)	(7)	(8)
Cyl. alignment	Optical	45	Fiducial model	$8.6^{+0.8}_{-0.8}$	$0.83^{\pm0.02}$	$-0.02^{\pm0.06}$	0.24
Cyl. alignment	Optical	45	Masked emission lines	$8.7^{+0.8}_{-0.8}$	$0.84^{\pm0.02}$	$-0.01^{\pm0.06}$	0.25
Cyl. alignment	Blue	45	–	$6.9^{+0.7}_{-0.7}$	$0.83^{\pm0.02}$	$-0.02^{\pm0.06}$	0.35
Cyl. alignment	CaT	45	–	$8.1^{+1.1}_{-1.0}$	$0.85^{\pm0.02}$	$-0.01^{\pm0.12}$	0.13
Cyl. alignment	Optical	89	–	$9.0^{+0.8}_{-0.8}$	$0.82^{\pm0.03}$	$-0.04^{\pm0.04}$	0.28
Cyl. alignment	Optical	45	F814 mass model	$8.6^{+1.2}_{-1.3}$	$3.33^{\pm0.12}$[a]	$-0.02^{\pm0.09}$	0.33
Cyl. alignment	Optical	45	Radially varying M/L	$7.3^{+1.2}_{-1.1}$	$0.80^{\pm0.02}$	$-0.02^{\pm0.07}$	0.20
Sph. alignment	Optical	45	Fiducial model	$4.6^{+2.5}_{-2.7}$	$0.86^{\pm0.02}$	$0.38^{\pm0.17}$	0.21
Sph. alignment	Optical	45	Masked emission lines	$4.7^{+2.1}_{-2.3}$	$0.87^{\pm0.02}$	$0.42^{\pm0.18}$	0.21
Sph. alignment	Blue	45	–	$2.9^{+1.8}_{-2.1}$	$0.86^{\pm0.02}$	$0.40^{\pm0.18}$	0.27
Sph. alignment	CaT	45	–	$4.1^{+2.3}_{-2.4}$	$0.87^{\pm0.03}$	$0.40^{\pm0.16}$	0.10
Sph. alignment	Optical	89	–	$4.8^{+1.6}_{-1.7}$	$0.84^{\pm0.03}$	$0.35^{\pm0.14}$	0.25
Sph. alignment	Optical	45	F814 mass model	$4.3^{+1.8}_{-1.8}$	$3.45^{\pm0.12}$[a]	$0.36^{\pm0.15}$	0.28
Sph. alignment	Optical	45	Radially varying M/L	$4.1^{+2.2}_{-1.8}$	$0.82^{\pm0.02}$	$0.30^{\pm0.16}$	0.18

Notes. Columns 1–4 show the inputs of the dynamical models; columns 5–8 show the JAM results. The tests are described in detail in Section 4.4.3. For each JAM run, we used the set-up explained in Section 4.3 with the kinematic uncertainties ($\delta_{\rm kin}$) enhanced for $R > 0.5$ arcsec. The reduced χ^2 values were calculated using the enhanced kinematic errors.
[a]This M/L is in the *i* band.

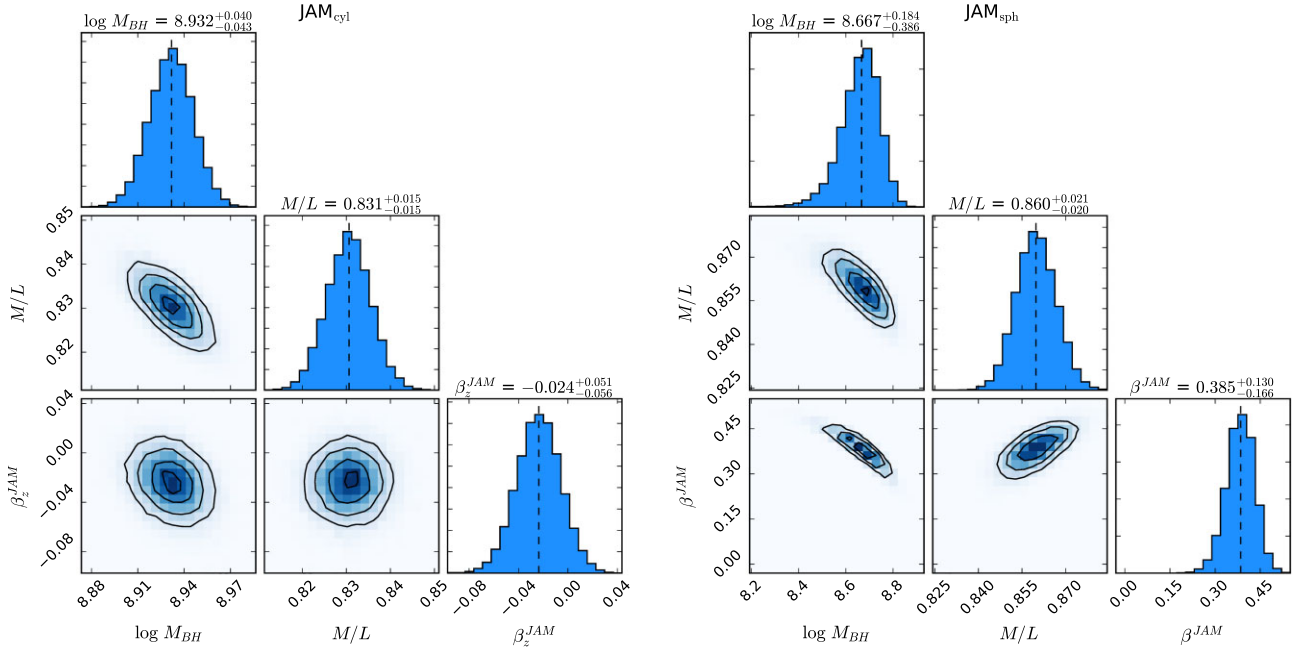

Figure C1. MCMC posterior probability distributions of the fiducial JAM models assuming a cylindrical (left) and spherical-aligned (right) velocity ellipsoid. The contour plots show the two-dimensional distributions for each parameter ($M_{\rm BH}$, M/L, β) combination, and the histograms show the projected one-dimensional distributions. The errors above the histograms are at 99.73 per cent confidence intervals, which corresponds to 3σ significance.

APPENDIX D: SCHWARZSCHILD + DARK MATTER GRIDS

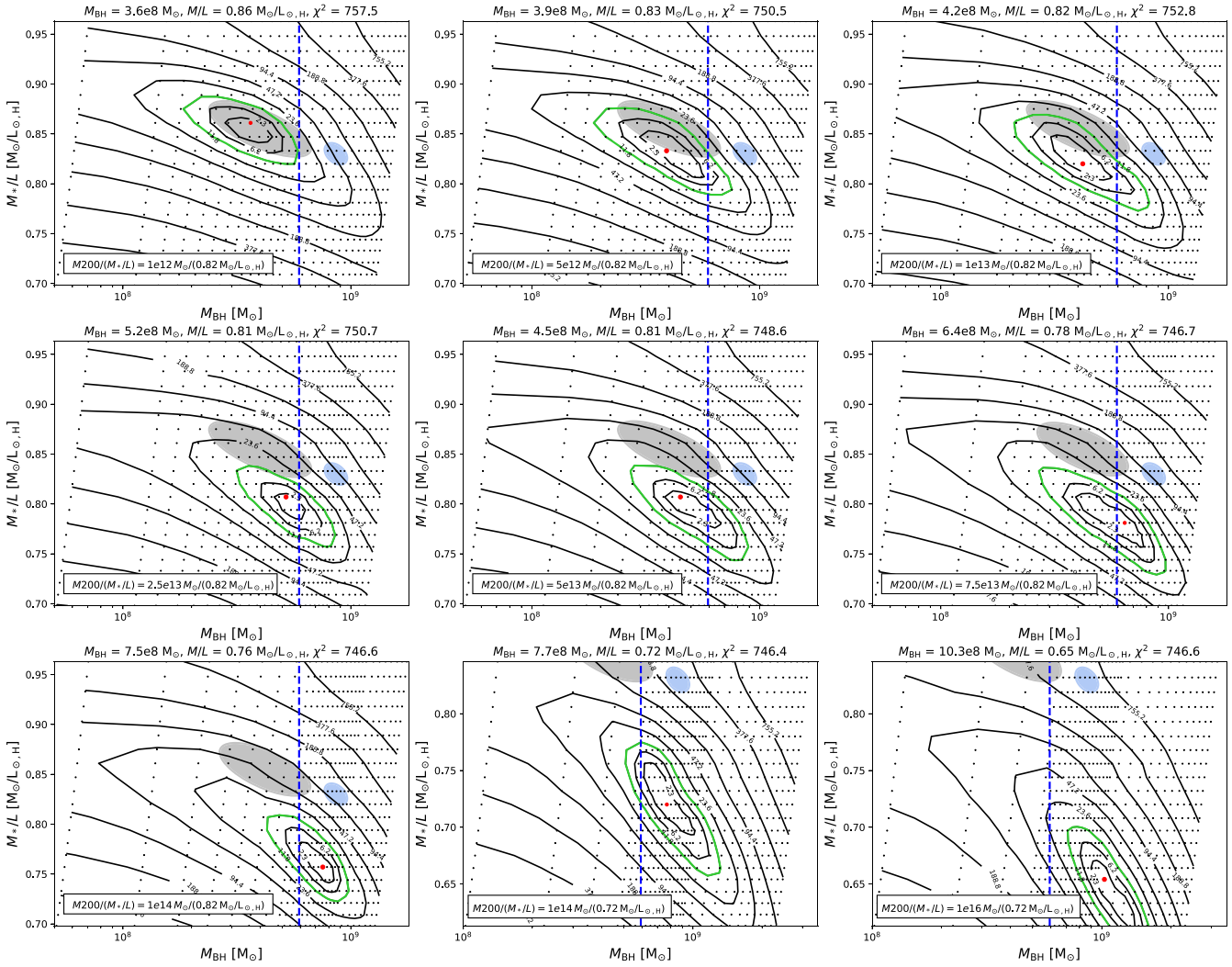

Figure D1. Results of our Schwarzschild run including a dark matter halo. In the runs, we have varied M_{BH}, M_*/L, and M_{200}. Each of the panels shows the M_{BH}–M_*/L grid (like Fig. 8) for an increasing dark matter fraction. While running Schwarzschild models, both M_{BH} and M_{200} need to be re-scaled for each model. The scale factor is the (M_*/L) of the grid divided by the starting (M_*/L) of the models. The confidence level was derived for each M_{BH}–M_*/L grid independently. As expected, with increasing dark matter fraction, the black hole mass increases and the M_*/L decreases. As expected, with increasing dark matter fraction, the black hole mass increases and the M/L decreases. Contrary to Fig. 8, here the M/L from JAM is larger or equal to that from Schwarzschild's models. This is because the former represents the total M/L, while the latter is that of the stellar component alone. When dark matter increases, the stellar M/L must decrease with respect to the total one, as observed.

This paper has been typeset from a TEX/LATEX file prepared by the author.